Colocalized, Bidirectional Optogenetic Modulations in Freely Behaving Animals with a Wireless Dual-Color Optoelectronic Probe

Lizhu Li,[1, #] Lihui Lu,[2, 3, #] Yuqi Ren,[2, 3] Guo Tang,[1] Yu Zhao,[1] Xue Cai,[1] Zhao Shi,[1] He Ding,[4] Changbo Liu,[5] Dali Cheng,[1] Yang Xie,[1] Huachun Wang,[1] Xin Fu,[6] Lan Yin,[6] Minmin Luo,[2, 3, 7, *] Xing Sheng [1, 7, *]

Affiliations

[1]Department of Electronic Engineering, Beijing National Research Center for Information Science and Technology, Center for Flexible Electronics Technology, Tsinghua University, Beijing, China

[2]Chinese Institute for Brain Research, Beijing, China

[3]National Institute of Biological Sciences and School of Life Sciences, Tsinghua University, Beijing, China

[4]Beijing Engineering Research Center of Mixed Reality and Advanced Display, School of Optics and Photonics, Beijing Institute of Technology, Beijing, China

[5]School of Materials Science and Engineering and Hangzhou Innovation Institute, Beihang University, Beijing, China

[6]School of Materials Science and Engineering, Tsinghua University, Beijing, China

[7]IDG/McGovern Institute for Brain Research, Tsinghua University, Beijing, China

# L. Li and L. Lu contributed equally to this work.

*Correspondence to: luominmin@cibr.ac.cn; xingsheng@tsinghua.edu.cn

ABSTRACT

The precise control of neural activities at both cellular and circuit levels reveals significant impacts on the fundamental neuroscience explorations and medical applications. Optogenetic methods provide efficient cell-specific modulations, but state-of-the-art technologies lack the ability of simultaneous neural activation and inhibition in a same brain region of freely moving animals. Here we report bidirectional neuronal activity manipulation accomplished by a wireless, dual-color optogenetic probe in synergy with the co-expression of two spectrally distinct opsins (ChrimsonR and stGtACR2) in a rodent model. Based on vertically assembled, thin-film microscale light-emitting diodes (micro-LEDs) on flexible substrates, the dual-color probe shows colocalized red and blue emissions and allows chronic *in vivo* operations with desirable biocompatibilities. In addition, we discover that neurons co-expressing the two opsins can be deterministically evoked or silenced under red or blue irradiations. Implanted in behaving mice, the wirelessly controlled dual-color probe interferes with dopaminergic neurons in the ventral tegmental area (VTA), increasing or decreasing dopamine levels with colocalized red and blue stimulations. Such bidirectional regulations further generate rewarding and aversive behaviors of freely moving animals in a place preference test. The technologies established here will create numerous opportunities and profound implications for the brain research.

INTRODUCTION

Understanding the brain functions and treating neurological disorders rely on the continuous development of advanced technologies to interrogate with the complex nervous systems[1, 2]. Over the past decades, optogenetic methods have been emerging as a powerful toolset for effective and precise neural manipulation, owing to their capability of specific cell targeting[3, 4]. Until now, a range of genetically encoded, light-sensitive proteins (opsins) with distinct spectral responses have been engineered to regulate flows of different cations and anions[5–16], triggering various biological responses, from cells and *C. elegans* to rodents and non-human primates[17–20]. Accompanying the development of opsins, advanced technologies for light delivery into the brain have also been progressing rapidly. Apart from various fiber-based emitters interfacing with external light sources[21–23], recently developed implantable probes based on thin-film, microscale optoelectronic devices have offered a viable solution to versatile neural modulations in untethered animals, when incorporated with wirelessly operated systems[24–26]. In addition to these achievements, bidirectional neural modulations, for example, by activating or suppressing the same or different populations of cells in behaving animals with light at different wavelengths, are still highly demanded. Such capabilities would enable more precise control of neural activities to advance both neuroscience explorations and disease medications[27]. Certain efforts have been attempted, including explorations based on experiments by expressing excitatory and inhibitory opsins in separate animals[28, 29] or distinct cells in different neural regions[17, 30]. There are few reports on dual-color optogenetic activation and inhibition by co-expressing different opsins in the same cells[31–33], but the efficacy and utility of such bidirectional modulations could be limited by the potential spectral overlay of the two opsins and the lack of miniaturized light delivery systems. Therefore, we envision that wirelessly operated light sources with polychromatic

65 emissions, which collaborate with co-expressed opsins, can be implemented for untethered
66 use in freely moving animals and enable previously inaccessible applications.

67 This study presents synergic optoelectronic and biological strategies to overcome
68 challenges of existing techniques, and realize colocalized, bidirectional neural manipulations
69 in untethered behaving animals. With heterogeneously integrated thin-film, microscale light-
70 emitting diodes (micro-LEDs), a wirelessly operated, implantable dual-color probe allows
71 independently controlled red and blue emissions in the same region. We also discover that the
72 co-expression of two channelrhodopsins (ChrimsonR and stGtACR2) in the same group of
73 neurons enables efficient light-evoked cell depolarization and hyperpolarization with
74 controlled cation and anion flows under red and blue illuminations, respectively. With the
75 wireless, dual-color micro-LED probes implanted into the ventral tegmental area (VTA) of
76 freely behaving mice, preference and aversion tests clearly demonstrate the bidirectional
77 optogenetic excitation and inhibition capability. Furthermore, *in vivo* behavioral results
78 associated with the red and blue stimulations in the VTA are validated by increased or
79 decreased dopamine levels detected in the nucleus accumbens (NAc) in real time.

80

81 **RESULTS**

82 **Wirelessly operated, dual-color micro-LED probes and circuit systems**

83 We design and implement a wireless, dual-color micro-LED probe that generates red
84 and blue emissions in the same brain region for bidirectional optogenetic modulations *in vivo*,
85 as schematically illustrated in Figure 1a. Specifically, with the co-expression of spectrally
86 distinct ion channels, ChrimsonR[7] and stGtACR2[9], in the same population of cells, red and
87 blue light regulate the inflow of cations and anions, causing cell depolarization and
88 hyperpolarization, respectively (Figure 1b). Figure 1c displays an exploded view of the dual-
89 color probe, with design and fabrication details provided in the supplemental information and

Figure S1. From bottom to top, the probe structure comprises a copper (Cu) coated polyimide (PI) thin-film substrate, an indium gallium phosphide (InGaP) red LED, a silicon oxide (SiO_2) / titanium oxide (TiO_2) based dielectric filter, an indium gallium nitride (InGaN) blue LED. All the devices (red LEDs, blue LEDs and filters) are formed in thin-film, microscale formats (lateral dimension ~ 125 μm × 180 μm, thickness ~ 5–7 μm) through epitaxial liftoff, and vertically assembled via transfer printing[34–36] (Figure 1d). The intrinsic optical transparency of active layers in the InGaN blue micro-LED allows emissions from the red micro-LED passing through with minimal losses. Additionally, the designed filter selectively reflects blue light and transmits red light, enhancing the emissive efficiencies of both micro-LEDs.

Flexible PI substrates with vertically stacked micro-LEDs are laser milled and encapsulated with a waterproof coating, forming a needle shaped probe with a dimension (thickness ~120 μm and width ~320 μm) similar to a conventional silica fiber (diameter ~220 μm) used in optogenetic stimulations. Separate metallization and electrical insulation ensure that red and blue micro-LEDs can be independently lighted up and display spectrally varied illuminations (red, blue or combined) in the same location (Figure 1e and Movie S1). Figure 1f plots measured electroluminescence (EL) spectra. The red and blue micro-LEDs exhibit emission peaks at 630 nm and 480 nm, which are in good accordance with the excitation spectra of ChrimsonR and stGtACR2 (data extracted from references[7, 8]), respectively. Moreover, the spectral separation between the two opsins, as well as their different operational modes (pulsed red light activation for ChrimsonR, and continuous blue light inhibition for stGtACR2), guarantee precise optogenetic activation and inhibition with minimal optical interferences. More optoelectronic properties of the dual-color micro-LED probe, including current-voltage characteristics, quantum efficiencies, power irradiance and angular-dependent emissive profiles are presented in Figure S2. Under injection currents of

114 10 mA, the red and the blue micro-LEDs can reach irradiances up to 50 mW/mm^2 and 200
115 mW/mm^2 on the device surface, which are sufficient for optogenetic modulations.

116 To illustrate the optical performance of the devices, we insert a dual-color probe into
117 a brain phantom (Figure 1g, top). For comparison, established models calculate optical
118 profiles based on the optical properties (absorption and scattering) of brain tissues (Figure 1g,
119 bottom). Both experimental and simulation results reveal that vertically stacked dual-color
120 micro-LEDs show colocalized red and blue emission profiles, ensuring effective activation
121 and inhibition in the same brain region. Power irradiances for blue and red emissions
122 decrease to 10% of the original power at propagating distances of ~400 μm and ~800 μm,
123 respectively. Such a unique design of vertical assembly holds prominent advantages
124 compared to a probe with laterally arranged red and blue micro-LEDs displaying highly
125 misaligned emissions, which could severely limit its capability for bidirectional modulations.

126 Thermal behaviors of the micro-LED probe are also systematically analyzed, with
127 detailed results presented in the supplemental material and Figure S3. Probes are inserted into
128 the brain phantom and the living mouse brain, with temperature rises measured by an infrared
129 camera and a thermocouple, respectively. Both experiments obtain similar results and are in
130 agreement with the thermal models established based on finite-element analysis. Under a
131 pulsed operation (20-Hz frequency, 10-ms pulse duration, current 0–10 mA), the tissue
132 temperature rises caused by the red micro-LED can be restricted within 1 °C. The operation
133 of the blue micro-LED induces a higher thermal effect, because practical neural inhibition for
134 stGtACR2 requires continuous current injection; nonetheless, the tissue heating can be
135 controlled within 2 °C by limiting the current within 5 mA. Such operation modes for red and
136 blue micro-LEDs will be employed throughout *in vivo* experiments, to mitigate undesired
137 neural responses and possible tissue damage due to overheating.

138 We also design a customized, miniaturized flexible circuit module wirelessly operate
139 the dual-color micro-LED probe. Controlled by radio frequency (RF) communication at 2.4
140 GHz, the battery-powered circuit (weight ~1.9 g) can independently address the red and the
141 blue micro-LEDs, by adjusting their pulse frequencies, durations and injection currents for
142 versatile neural modulations *in vivo* (Figure 1h, and details in the supplemental material and
143 Figures S4–S7). Designed programming commends also allow the independent operation of
144 multiple micro-LED probes in synchronized or non-synchronized modes (Movie S2). After
145 subcranially implanting the micro-LED probe into a behaving mouse, the light-weighted
146 circuit mounted onto the mouse head provides the capability for optogenetic control in an
147 untethered manner (Figure 1i).
148

149 **Bidirectional optogenetic manipulations of neurons *in vitro*, with dual-color stimulations**

150 We first evaluate the feasibility of dual-color, bidirectional optogenetic modulations for
151 neurons co-expressing ChrimsonR and stGtACR2 in brain slices with electrophysiological
152 tests. Mixed vectors of AAV-CAG-DIO-ChrimsonR-mCherry and AAV-EF1a-DIO-
153 stGtACR2-EGFP are injected into the ventral tegmental area (VTA) of *DAT-Cre* mice
154 (Figure 2a). The deployment of the soma-targeted variant stGtACR2 exhibits performance
155 superior to previously reported anion channel GtACR2, by enhancing the membrane
156 trafficking and reducing the axonal excitation[8, 9]. Figure 2b shows the fluorescence images of
157 stained cells 3 weeks after viral injection in the VTA, including 4',6-diamidino-2-
158 phenylindole (DAPI, blue), stGtACR2 (green) and ChrimsonR (red). The merged graph and
159 zoomed in views (Figure 2c) clearly reveal the desirable co-expression of the two opsins in
160 target cells. Statistical results show that ~30% of cells are labeled with stGtACR2 or
161 ChrimsonR, and > 83% of cells co-express both opsins (Figure 2d).

162 Whole-cell patch recordings capture intracellular signals of these cells under optical
163 stimulations (Figure 2e). Other than using our designed micro-LED probe, here we employ a
164 collimated light spot with coupled red (633 nm) and blue (480 nm) laser sources for *in vitro*
165 experiments, to achieve uniform illuminations for better power calibrations. Figures 2f and 2g
166 validate that pulsed red stimulations (20-Hz frequency, 10-ms pulse duration) induce action
167 potentials (APs or spikes) by depolarizing these cells, and spike activation probability
168 increases at elevated red irradiances. In these same cells, continuous blue stimulations
169 suppress activities by hyperpolarization (Figures 2h–2j). Voltage clamp results illustrate that
170 blue light evokes photocurrent reversion when the membrane potential becomes more
171 positive (Figure 2h), and probability for spike inhibition also increases at elevated blue
172 irradiances (Figures 2i and 2j). Threshold irradiances for complete spike activation and
173 inhibition are around 10 mW/mm^2 and 1 mW/mm^2 for red and blue illuminations,
174 respectively. The results are consistent with previous reports on cells expressing only
175 ChrimsonR or stGtACR2[7, 9].

176 Notably, we do not only demonstrate that the co-expression of both opsins does not
177 affect the efficacy of cell activity excitation or suppression, but also accomplish bidirectional
178 activation and inhibition in the same cell by instantaneously altered red and blue irradiations
179 (Figure 2k). In accordance with activation spectra of two opsins (Figure 1f), red light does
180 not interact with stGtACR2, which exhibits nearly zero responses at wavelengths longer than
181 600 nm. On the other hand, ChrimsonR should have responded to blue light, which could
182 raise concern about possible optical crosstalk. Nevertheless, spike activations caused by blue
183 light do not occur in cells co-expressing ChrimsonR and stGtACR2, since cell suppressions
184 by turning on stGtACR2 channels arise and saturate at a much lower blue irradiance. This
185 fact can be confirmed by patching the cells under combined red and blue illuminations
186 (Figures 2l and 2m). Example traces in Figure 2l show that red-light-evoked spikes are

suppressed under simultaneous blue illuminations even with very low irradiances. More traces are reported in Figure S8, and Figure 2m summarizes the spike probability (measured and averaged among n = 5 cells) with combined red and blue illuminations. Introducing blue irradiances orders of magnitude lower than red irradiances can effectively suppress cell spikes and cause activity inhibition.

Bidirectional optogenetic modulation of preference and aversion behaviors *in vivo*, with wireless dual-color micro-LED probes

Activities of the dopaminergic neurons in the VTA we manage to manipulate in Figure 2 significantly correlate with the reward and aversion based behaviors[37, 38, 39]. In Figure 3, we further exploit the capability of bidirectional optogenetic manipulations by implanting dual-color micro-LED probes into behaving animals. After the injection of AAV-CAG-DIO-ChrimsonR-mCherry and AAV-EF1a-DIO-stGtACR2-EGFP vectors, the dual-color micro-LED probe is implanted into the VTA of *DAT-cre* mice (Figure 3a). Figure 3b illustrates the locations of the micro-LEDs in the VTA, with a slice showing the co-expression of ChrimsonR and stGtACR2, combined with the luminescence of the red and the blue micro-LEDs under corresponding optical excitations. To access the devices' biocompatibility *in vivo*, histological examinations of brain slices show that inflammatory reactions of the micro-LED probe are similar to a conventional silica fiber (diameter ~220 μm) 1 day or 3 weeks post implantation (Figure S9), owing to its thin-film geometry, mechanical flexibility and bio-friendly encapsulation. Furthermore, the parylene-based, waterproof encapsulation maintains the micro-LEDs' chronic and stable operation for more than 200 days after implantation (Figure S10).

210 *In vivo* experiments are performed within a real-time place preference / avoidance
211 (RTPP) paradigm. After 14 days of virus and micro-LED probe injection, we place mice in a
212 two-compartment apparatus and monitor their behaviors with a camera during optogenetic
213 modulations (Figure 3c and Figure S11). Figure 3d provides the test protocol, including a
214 baseline pretest (10 mins), red LED stimulation (pulsed wave, 30 mins), a rest phase (30
215 mins), and blue LED stimulation (continuous wave, 30 mins). Representative heat maps in
216 Figure 3e show the change of real-time behaviors during optogenetic stimulations, for mice
217 expressing different combinations of opsins. Summarized results in Figure 3f clearly show
218 that animals co-expressing ChimsonR and stGtACR2 present strong preference and
219 avoidance behaviors following red and blue stimulations, respectively.

220 By contrast, the control groups without photosensitive opsins (expressing only EGFP
221 and mCherry) show little difference of behaviors under optical stimulations. More results are
222 provided in Figures S12 and S13, comparing these animals with other group expressing only
223 ChrimsonR or stGtACR2. When introducing only ChrimsonR, animals exhibit place
224 preference under both red and blue stimulations. For the group with only stGtACR2, blue
225 light effectively evokes place aversion while red light generates little influence on animal
226 behaviors. Figures 3g and 3h present the dynamic behavior change at different time courses.
227 These results are consistent with the spectral characteristics of the opsins as well as the *in*
228 *vitro* neural responses at the cellular level (Figure 2), elucidating the utility of bidirectional
229 modulations with wireless, dual-color micro-LED probes. In conclusion, the implantable
230 wireless dual-color LED probe combining with two spectrally distinct channerhodopins can
231 realize bi-directional control the place preference or aversion in freely behaving mice.

232

233 **Bidirectional optogenetic regulation of dopamine release *in vivo*, with wireless dual-**
234 **color micro-LED probes**

235 The effective bidirectional behavior manipulations demonstrated in Figure 3 can be ascribed
236 to the light induced activation and inhibition of dopaminergic neurons in the VTA. We
237 further investigate the effect of optogenetic stimulations on the dopamine release using *in*
238 *vivo* experiments described in Figure 4a. Similarly, combined opsins are expressed and
239 followed by implanting the dual-color micro-LED probe in the VTA of *DAT-cre* mice. While
240 stimulations are performed in the VTA, dopamine signals are simultaneously monitored in
241 one of its main projection areas, the nucleus accumbens (NAc)[40, 41, 42]. A genetically encoded
242 indicator $GRAB_{DA2m}$[43] is expressed in the NAc, where the fluorescence signals are recorded
243 with a fiber photometer[28, 29, 39, 44, 45, 46]. The combination of micro-LED based optogenetic
244 stimulations and fiber based photometric recordings realizes all-optical interrogation of
245 neural circuits. During the surgery, we carefully select the insertion direction of the micro-
246 LED probe, in order to obtain desirable stimulation efficacy in the VTA and minimize the
247 optical crosstalk that could disturb photometric recording in the NAc (Figure S14).
248 Fluorescence images in Figure 4b show the expressions of $GRAB_{DA2m}$ in the NAc as well as
249 ChrimsonR and stGtACR2 in the VTA.

250 Figure 4c plots temporally resolved dopamine release in respond to stimulations
251 caused by red and blue micro-LEDs in a same mouse. More representative curves are
252 presented in Figure S15, with results summarized in Figure 4d. Illuminating the VTA by red
253 or blue micro-LEDs (with injection currents from 0 to 10 mA) clearly induces increased or
254 decreased dopamine signals in the NAc, which correlates with neuron responses at the
255 cellular level (Figure 2). Experiments operated among animal groups expressing different
256 opsins are also performed, with results compared in Figure 4e. In contrast to the group
257 expressing both opsins (ChrimsonR and stGtACR2), mice with only ChrimsonR show
258 increased dopamine release under both red and blue illuminations, and dopamine suppression
259 is observed under blue illumination for the mice with only stGtACR2. The control group

260 (with EGFP and mCherry) exhibits no response under optical stimulations. These results
261 evidently explain *in vivo* preference and avoidance behaviors presented in Figure 3,
262 showcasing the capability for precise control of neural activities based on bidirectional, dual-
263 color modulations.

264 We further investigate neural activities with coincident red and blue LED radiations.
265 Figure 4f plots example traces of dopamine transients, in response to the red and blue micro-
266 LEDs under pulse and continuous operations (6-s duration) with varied currents. Statistical
267 data for accumulative dopamine concentration variations (unit: area under the curve during
268 stimulation, or AUC) are summarized in Figure 4g and Figure S16. Decreasing power of the
269 red LED and increasing the power of the blue LED cause the decline of dopamine release.
270 Additionally, the blue LED current required to suppress the dopamine release is much lower
271 than that of the red LED required for dopamine level rises, which further confirms with the
272 cellular activities reported in Figure 2.

273 Figure 4h (and more examples in Figure S17) presents dopamine dynamics in
274 response to alternated or combined red and blue LED stimulations, for mice expressing
275 ChrimsonR and stGtACR2. The red illumination triggers the elevated dopamine release,
276 while the use of blue light can effectively and promptly suppress the signal. Similar
277 illumination patterns are implemented on animals expressing different opsins (Figure S18)
278 and results are summarized and compared in Figures 4i–4k. Evidently, red or blue
279 illuminations bidiretionally regulate dopamine signals in the experiment group (with both
280 ChrimsonR and stGtACR2). On the other hand, animals expressing only ChrimsonR can be
281 excited by both red and blue light, and those with only stGtACR2 can only be inhibited by
282 blue light and show no reaction under red light. Finally, the control group (with EGFP and
283 mCherry) does not respond to any optical stimulation patterns. Taken together, these results
284 clearly demonstrate that wireless dual-color LED combined with optogenetics enable

285 efficient, bidirectional control of neuronal activity in the VTA and DA release of the terminal
286 in the NAc.

287

288 **DISCUSSION**

289 Optogenetic modulations offer a viable solution for cell-type-specific targeting, but still
290 demand biological and engineering tools for versatile functionalities. In this work, we report
291 that bidirectional optogenetic activation and inhibition in behaving animals can be achieved
292 by co-expressing spectrally distinct excitatory and inhibitory channelrhodopsins, cooperating
293 with a wireless, dual-color micro-LED probe for colocalized red and blue stimulations. With
294 collective results at cellular, circuit and behavioral levels, successful proof-of-concept
295 demonstrations in the VTA-NAc circuitry in freely moving mice clearly establish the utility
296 of such a synergistic methodology.

297 The unique characteristics of thin-film, microscale optoelectronic devices and their
298 integration strategies implicate prominent advantages over conventional fibers or single color
299 LED sources. In terms of technology developments, more directions can be explored and
300 some preliminary efforts are presented below: 1) Multiple red and blue micro-LEDs can be
301 assembled on the implantable probe via the stacking approach, realizing multi-channel,
302 bidirectional modulations imposed on multiple brain regions (Movie S3). It is noted that the
303 efficacy of preference behavior regulations demonstrated in Figure 3 would also be enhanced
304 by implementing dual channel stimulations bilaterally in the VTA[47, 48, 49, 50]. 2) The use of
305 miniaturized wireless control circuits allows independently addressing multiple, untethered
306 animal objects, making the interrogations of complex social behaviors more feasible (Movie
307 S4)[51, 52, 53, 54]. 3) Micro-LEDs with other colors can also be included and target on specific
308 opsins more efficiently. For example, a tri-color probe can be achieved by similarly stacking
309 red, green and blue micro-LEDs in a vertical structure (Movie S5). Independently controlled

310 micro-LEDs can interact with different opsins that express in the same or different
311 populations of cells. 4) Micro-LED based optogenetics can also be combined with previously
312 reported electrical, optical and chemical sensors as well as microchannel devices for drug
313 administrations[55, 56, 57, 58], achieving closed-loop neural activity stimulations and detections.
314 Taken together, we envision a multi-spectral, multi-channel, multi-objective and multi-
315 functional optical neural interface, realizing wireless, real-time, bi-directional, close-loop and
316 simultaneous interrogations of neural signals in living animals.

317 On the other hand, the efficacy of optogenetic modulations can be further optimized
318 by advanced biological engineering. A recent effort fuses excitatory and inhibitory
319 channelrhodopsins (ChrimsonR and GtACR2) in a single, trafficking-optimized tandem
320 protein (BiPOLES), improving the efficiency of opsin co-expression[59]. In addition to the
321 bidirectional modulation of a same cell population, the dual-color (or even tri-color) micro-
322 LED probe can also selectively activate genetically distinct and spatially intermingled cells
323 expressing spectrally resolved opsins (for example, blue for ChR2 or GtACR2, green for
324 C1V1 or GtACR1 and red for ChrimsonR or halorhodopsin)[3, 7, 8, 22] and provide prolonged
325 activation of neuronal activity by regulating step-function opsins (for example, SSFO and
326 SOUL)[11, 13, 60], which is also of critical importance for understanding the circuit structures
327 and functions. Possible applications would include bidirectional modulations of neural
328 activities by leveraging electrophysiological or neurotransmitter signals for medications of
329 seizures or Parkinson's disease[27, 61, 62]. Besides central nervous systems, peripheral neural
330 circuits can also be targeted for medical treatments[63, 64]. In summary, the results presented
331 here provide a viable means for fundamental neuroscience studies and advanced
332 neuroengineering applications.

333 **REFERENCES**

334 1. Won SM, Song E, Reeder JT, Rogers JA. Emerging modalities and implantable
335 technologies for neuromodulation. *Cell* 2020, **181**(1)**:** 115-135.

336 2. Vázquez-Guardado A, Yang Y, Bandodkar AJ, Rogers JA. Recent advances in
337 neurotechnologies with broad potential for neuroscience research. *Nat Neurosci* 2020,
338 **23**(12)**:** 1522-1536.

339 3. Boyden ES, Zhang F, Bamberg E, Nagel G, Deisseroth K. Millisecond-timescale,
340 genetically targeted optical control of neural activity. *Nat Neurosci* 2005, **8**(9)**:** 1263-
341 1268.

342 4. Zhang F, Wang L-P, Brauner M, Liewald JF, Kay K, Watzke N*, et al.* Multimodal
343 fast optical interrogation of neural circuitry. *Nature* 2007, **446**(7136)**:** 633-639.

344 5. Yizhar O, Fenno LE, Davidson TJ, Mogri M, Deisseroth K. Optogenetics in neural
345 systems. *Neuron* 2011, **71**(1)**:** 9-34.

346 6. Chow BY, Han X, Dobry AS, Qian X, Chuong AS, Li M*, et al.* High-performance
347 genetically targetable optical neural silencing by light-driven proton pumps. *Nature*
348 2010, **463**(7277)**:** 98-102.

349 7. Klapoetke NC, Murata Y, Kim SS, Pulver SR, Birdsey-Benson A, Cho YK*, et al.*
350 Independent optical excitation of distinct neural populations. *Nat Methods* 2014,
351 **11**(3)**:** 338-346.

352 8. Govorunova EG, Sineshchekov OA, Janz R, Liu X, Spudich JL. Natural light-gated
353 anion channels: A family of microbial rhodopsins for advanced optogenetics. *Science*
354 2015, **349**(6248)**:** 647.

355 9. Mahn M, Gibor L, Patil P, Cohen-Kashi Malina K, Oring S, Printz Y*, et al.* High-
356 efficiency optogenetic silencing with soma-targeted anion-conducting
357 channelrhodopsins. *Nat Commun* 2018, **9**(1)**:** 4125.

358 10. Zhang F, Prigge M, Beyriere F, Tsunoda SP, Mattis J, Yizhar O*, et al.* Red-shifted
359 optogenetic excitation: a tool for fast neural control derived from Volvox carteri. *Nat*
360 *Neurosci* 2008, **11**(6)**:** 631-633.
361 11. Berndt A, Yizhar O, Gunaydin LA, Hegemann P, Deisseroth K. Bi-stable neural state
362 switches. *Nat Neurosci* 2009, **12**(2)**:** 229-234.
363 12. Hochbaum DR, Zhao Y, Farhi SL, Klapoetke N, Werley CA, Kapoor V*, et al.* All-
364 optical electrophysiology in mammalian neurons using engineered microbial
365 rhodopsins. *Nat methods* 2014, **11**(8)**:** 825-833.
366 13. Gong X, Mendoza-Halliday D, Ting JT, Kaiser T, Sun X, Bastos AM*, et al.* An ultra-
367 sensitive step-function opsin for minimally invasive optogenetic stimulation in mice
368 and macaques. *Neuron* 2020, **107**(1)**:** 38-51.
369 14. Brown J, Behnam R, Coddington L, Tervo DGR, Martin K, Proskurin M*, et al.*
370 Expanding the optogenetics toolkit by topological inversion of rhodopsins. *Cell* 2018,
371 **175**(4)**:** 1131-1140.
372 15. Chuong AS, Miri ML, Busskamp V, Matthews GAC, Acker LC, Sørensen AT*, et al.*
373 Noninvasive optical inhibition with a red-shifted microbial rhodopsin. *Nat Neurosci*
374 2014, **17**(8)**:** 1123-1129.
375 16. Chuong AS, Miri ML, Busskamp V, Matthews GAC, Acker LC, Sørensen AT*, et al.*
376 Noninvasive optical inhibition with a red-shifted microbial rhodopsin. *Nature*
377 *neuroscience* 2014, **17**(8)**:** 1123-1129.
378 17. Schild LC, Glauser DA. Dual Color Neural Activation and Behavior Control with
379 Chrimson and CoChR in Caenorhabditis elegans. *Genet* 2015, **200**(4)**:** 1029-1034.
380 18. Maimon BE, Sparks K, Srinivasan S, Zorzos AN, Herr HM. Spectrally distinct
381 channelrhodopsins for two-colour optogenetic peripheral nerve stimulation. *Nat*
382 *Biomed Eng* 2018, **2**(7)**:** 485-496.

383 19. Lu Y, Truccolo W, Wagner FB, Vargas-Irwin CE, Ozden I, Zimmermann JB*, et al.*
384 Optogenetically induced spatiotemporal gamma oscillations and neuronal spiking
385 activity in primate motor cortex. *J Neurosci* 2015, **113**(10)**:** 3574-3587.
386 20. Galvan A, Caiola MJ, Albaugh DL. Advances in optogenetic and chemogenetic
387 methods to study brain circuits in non-human primates. *J Neural Transm* 2018,
388 **125**(3)**:** 547-563.
389 21. Park S, Loke G, Fink Y, Anikeeva P. Flexible fiber-based optoelectronics for neural
390 interfaces. *Chem Rev* 2019, **48**(6)**:** 1826-1852.
391 22. Yizhar O, Fenno LE, Prigge M, Schneider F, Davidson TJ, O'Shea DJ*, et al.*
392 Neocortical excitation/inhibition balance in information processing and social
393 dysfunction. *Nature* 2011, **477**(7363)**:** 171-178.
394 23. Kampasi K, English DF, Seymour J, Stark E, McKenzie S, Voroslakos M*, et al.* Dual
395 color optogenetic control of neural populations using low-noise, multishank
396 optoelectrodes. *Microsyst Nanoeng* 2018, **4:** 1-16.
397 24. Kim T-i, McCall JG, Jung YH, Huang X, Siuda ER, Li Y*, et al.* Injectable, Cellular-
398 Scale Optoelectronics with Applications for Wireless Optogenetics. *Science* 2013,
399 **340**(6129)**:** 211.
400 25. Montgomery KL, Yeh AJ, Ho JS, Tsao V, Mohan Iyer S, Grosenick L*, et al.*
401 Wirelessly powered, fully internal optogenetics for brain, spinal and peripheral
402 circuits in mice. *Nat Methods* 2015, **12**(10)**:** 969-974.
403 26. Shin G, Gomez AM, Al-Hasani R, Jeong YR, Kim J, Xie Z*, et al.* Flexible Near-Field
404 Wireless Optoelectronics as Subdermal Implants for Broad Applications in
405 Optogenetics. *Neuron* 2017, **93**(3)**:** 509-521.e503.
406 27. Wykes RC, Kullmann DM, Pavlov I, Magloire V. Optogenetic approaches to treat
407 epilepsy. *J Neurosci Methods* 2016, **260:** 215-220.

408 28. Li Y, Zeng J, Zhang J, Yue C, Zhong W, Liu Z*, et al.* Hypothalamic circuits for
409 predation and evasion. *Neuron* 2018, **97**(4)**:** 911-924.
410 29. Lu L, Ren Y, Yu T, Liu Z, Wang S, Tan L*, et al.* Control of locomotor speed, arousal,
411 and hippocampal theta rhythms by the nucleus incertus. *Nat Commun* 2020, **11**(1)**:** 1-
412 16.
413 30. Roseberry TK, Lee AM, Lalive AL, Wilbrecht L, Bonci A, Kreitzer AC. Cell-Type-
414 Specific Control of Brainstem Locomotor Circuits by Basal Ganglia. *Cell* 2016,
415 **164**(3)**:** 526-537.
416 31. Gradinaru V, Zhang F, Ramakrishnan C, Mattis J, Prakash R, Diester I*, et al.*
417 Molecular and cellular approaches for diversifying and extending optogenetics. *Cell*
418 2010, **141**(1)**:** 154-165.
419 32. Stuber GD, Sparta DR, Stamatakis AM, van Leeuwen WA, Hardjoprajitno JE, Cho S*,*
420 *et al.* Excitatory transmission from the amygdala to nucleus accumbens facilitates
421 reward seeking. *Nature* 2011, **475**(7356)**:** 377-380.
422 33. Noked O, Levi A, Someck S, Amber-Vitos O, Stark E. Bidirectional optogenetic
423 control of inhibitory neurons in freely-moving mice. *IEEE Transactions on*
424 *Biomedical Engineering* 2020.
425 34. Li L, Liu C, Su Y, Bai J, Wu J, Han Y*, et al.* Heterogeneous Integration of Microscale
426 GaN Light-Emitting Diodes and Their Electrical, Optical, and Thermal
427 Characteristics on Flexible Substrates. *Adv Mater Technol* 2018, **3**(1)**:** 1700239.
428 35. Liu C, Zhang Q, Wang D, Zhao G, Cai X, Li L*, et al.* High Performance,
429 Biocompatible Dielectric Thin-Film Optical Filters Integrated with Flexible
430 Substrates and Microscale Optoelectronic Devices. *Adv Opt Mater* 2018, **6**(15)**:**
431 1800146.

432 36. Ding H, Lu L, Shi Z, Wang D, Li L, Li X, *et al.* Microscale optoelectronic infrared-
433 to-visible upconversion devices and their use as injectable light sources. *Proc Natl*
434 *Acad Sci U S A* 2018, **115**(26)**:** 6632-6637.
435 37. Lammel S, Lim BK, Malenka RC. Reward and aversion in a heterogeneous midbrain
436 dopamine system. *Neuropharmacology* 2014, **76:** 351-359.
437 38. Morales M, Margolis EB. Ventral tegmental area: cellular heterogeneity, connectivity
438 and behaviour. *Nat Rev Neurosci* 2017, **18**(2)**:** 73.
439 39. Cohen JY, Haesler S, Vong L, Lowell BB, Uchida N. Neuron-type-specific signals
440 for reward and punishment in the ventral tegmental area. *Nature* 2012, **482**(7383)**:** 85-
441 88.
442 40. Al-Hasani R, McCall JG, Shin G, Gomez AM, Schmitz GP, Bernardi JM, *et al.*
443 Distinct Subpopulations of Nucleus Accumbens Dynorphin Neurons Drive Aversion
444 and Reward. *Neuron* 2015, **87**(5)**:** 1063-1077.
445 41. Sun F, Zeng J, Jing M, Zhou J, Feng J, Owen SF, *et al.* A Genetically Encoded
446 Fluorescent Sensor Enables Rapid and Specific Detection of Dopamine in Flies, Fish,
447 and Mice. *Cell* 2018, **174**(2)**:** 481-496 e419.
448 42. Yuan L, Dou YN, Sun YG. Topography of Reward and Aversion Encoding in the
449 Mesolimbic Dopaminergic System. *J Neurosci* 2019, **39**(33)**:** 6472-6481.
450 43. Sun F, Zhou J, Dai B, Qian T, Zeng J, Li X, *et al.* Next-generation GRAB sensors for
451 monitoring dopaminergic activity in vivo. *Nat Methods* 2020, **17**(11)**:** 1156-1166.
452 44. Gunaydin Lisa A, Grosenick L, Finkelstein Joel C, Kauvar Isaac V, Fenno Lief E,
453 Adhikari A, *et al.* Natural Neural Projection Dynamics Underlying Social Behavior.
454 *Cell* 2014, **157**(7)**:** 1535-1551.
455 45. Lin R, Liang J, Wang R, Yan T, Zhou Y, Liu Y, *et al.* The Raphe Dopamine System
456 Controls the Expression of Incentive Memory. *Neuron* 2020, **106**(3)**:** 498-514.e498.

457 46. Cui G, Jun SB, Jin X, Pham MD, Vogel SS, Lovinger DM*, et al.* Concurrent
458 activation of striatal direct and indirect pathways during action initiation. *Nature*
459 2013, **494**(7436)**:** 238-242.
460 47. Yuan L, Liang T-Y, Deng J, Sun Y-G. Dynamics and functional role of dopaminergic
461 neurons in the ventral tegmental area during itch processing. *J Neurosci Res* 2018,
462 **38**(46)**:** 9856-9869.
463 48. Li Y, Li C-Y, Xi W, Jin S, Wu Z-H, Jiang P*, et al.* Rostral and caudal ventral
464 tegmental area GABAergic inputs to different dorsal raphe neurons participate in
465 opioid dependence. *Neuron* 2019, **101**(4)**:** 748-761.
466 49. Taylor NE, Van Dort CJ, Kenny JD, Pei J, Guidera JA, Vlasov KY*, et al.* Optogenetic
467 activation of dopamine neurons in the ventral tegmental area induces reanimation
468 from general anesthesia. *Proc Natl Acad Sci USA* 2016, **113**(45)**:** 12826-12831.
469 50. Chang CY, Gardner M, Di Tillio MG, Schoenbaum G. Optogenetic blockade of
470 dopamine transients prevents learning induced by changes in reward features. *Curr*
471 *Biol* 2017, **27**(22)**:** 3480-3486.
472 51. de Chaumont F, Ey E, Torquet N, Lagache T, Dallongeville S, Imbert A*, et al.* Real-
473 time analysis of the behaviour of groups of mice via a depth-sensing camera and
474 machine learning. *Nat Biomed Eng* 2019, **3**(11)**:** 930-942.
475 52. Kingsbury L, Huang S, Raam T, Letizia SY, Wei D, Hu RK*, et al.* Cortical
476 representations of conspecific sex shape social behavior. *Neuron* 2020, **107**(5)**:** 941-
477 953.
478 53. Kingsbury L, Huang S, Wang J, Gu K, Golshani P, Wu YE*, et al.* Correlated neural
479 activity and encoding of behavior across brains of socially interacting animals. *Cell*
480 2019, **178**(2)**:** 429-446.

481 54. Hong W, Kim D-W, Anderson DJ. Antagonistic control of social versus repetitive
482 self-grooming behaviors by separable amygdala neuronal subsets. *Cell* 2014, **158**(6)**:**
483 1348-1361.
484 55. Chiang C-H, Won SM, Orsborn AL, Yu KJ, Trumpis M, Bent B*, et al.* Development
485 of a neural interface for high-definition, long-term recording in rodents and nonhuman
486 primates. *Sci Transl Med* 2020, **12**(538)**:** eaay4682.
487 56. Qazi R, Gomez AM, Castro DC, Zou Z, Sim JY, Xiong Y*, et al.* Wireless optofluidic
488 brain probes for chronic neuropharmacology and photostimulation. *Nat Biomed Eng*
489 2019, **3**(8)**:** 655-669.
490 57. Lu L, Gutruf P, Xia L, Bhatti DL, Wang X, Vazquez-Guardado A*, et al.* Wireless
491 optoelectronic photometers for monitoring neuronal dynamics in the deep brain. *Proc*
492 *Natl Acad Sci USA* 2018, **115**(7)**:** E1374-E1383.
493 58. Liu C, Zhao Y, Cai X, Xie Y, Wang T, Cheng D*, et al.* A wireless, implantable
494 optoelectrochemical probe for optogenetic stimulation and dopamine detection.
495 *Microsyst Nanoeng* 2020, **6**(1)**:** 1-12.
496 59. Vierock J, Rodriguez-Rozada S, Pieper F, Dieter A, Bergs A, Zeitzschel N*, et al.*
497 BiPOLES: a tool for bidirectional dual-color optogenetic control of neurons. *BioRxiv*
498 2020. https://doi.org/10.1101/2020.07.15.204347
499 60. Selimbeyoglu A, Kim CK, Inoue M, Lee SY, Hong ASO, Kauvar I*, et al.* Modulation
500 of prefrontal cortex excitation/inhibition balance rescues social behavior in
501 CNTNAP2-deficient mice. *SCI TRANSL MED* 2017, **9**(401)**:** eaah6733.
502 61. Chen S, Weitemier AZ, Zeng X, He L, Wang X, Tao Y*, et al.* Near-infrared deep
503 brain stimulation via upconversion nanoparticle–mediated optogenetics. *Science*
504 2018, **359**(6376)**:** 679.

505 62. Kravitz AV, Freeze BS, Parker PRL, Kay K, Thwin MT, Deisseroth K*, et al.*
506 Regulation of parkinsonian motor behaviours by optogenetic control of basal ganglia
507 circuitry. *Nature* 2010, **466**(7306)**:** 622-626.
508 63. Keppeler D, Schwaerzle M, Harczos T, Jablonski L, Dieter A, Wolf B*, et al.*
509 Multichannel optogenetic stimulation of the auditory pathway using microfabricated
510 LED cochlear implants in rodents. *Sci Transl Med* 2020, **12**(553)**:** eabb8086.
511 64. Michoud F, Seehus C, Schönle P, Brun N, Taub D, Zhang Z*, et al.* Epineural
512 optogenetic activation of nociceptors initiates and amplifies inflammation. *Nat*
513 *Biotechnol* 2021, **39**(2)**:** 179-185.

Acknowledgements

This work is supported by National Natural Science Foundation of China (NSFC) (61874064), Beijing Municipal Natural Science Foundation (4202032), Beijing Innovation Center for Future Chips at Tsinghua University, Center for Flexible Electronics Technology at Tsinghua University, Beijing National Research Center for Information Science and Technology (BNR2019ZS01005). We thank Prof. Y. Li (Peking University) for support on $GRAB_{DA2m}$, Y. Zhou and Y. Ju (Chinese Institute for Brain Research, Beijing) for support on stGtACR2.

Author contributions

X. S. and M. L. developed the concepts. L. Li, G. T., Y. Z., X. C., Z. S., H. D., C. L., Y. X., H. W., L. Y. and X. S. performed material, device and circuit design, fabrication and characterization. L. Li, X. C., D. C, and X. S. performed the simulations. L. Li, L. Lu, Y. R., G. T., X. F., L. Y., M. L., and X. S. designed and performed biological experiments. L. Li, L. Lu, M. L. and X. S. wrote the paper in consultation with other authors.

Competing interests

The authors declare no competing interests.

Data and materials availability

All data needed to evaluate the conclusions in the paper are present in the paper and/or the Supplementary information.

Figure 1

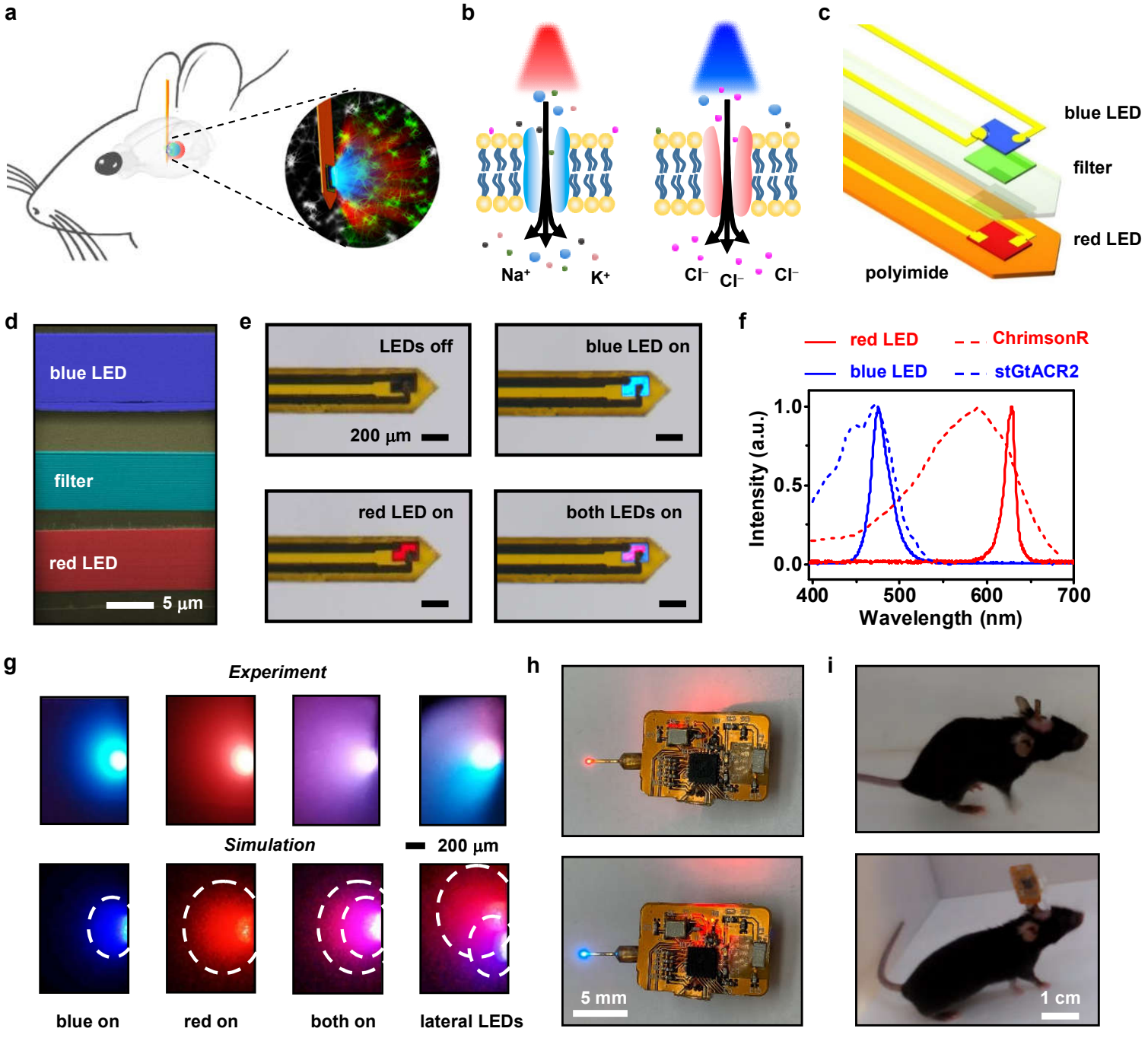
a
b
Na+
K+
Cl−
Cl−
Cl−
c
blue LED
filter
red LED
polyimide
d
blue LED
filter
red LED
5 µm
e
LEDs off
200 µm
blue LED on
red LED on
both LEDs on
f
red LED
ChrimsonR
blue LED
stGtACR2
Intensity (a.u.)
1.0
0.5
0.0
400
500
600
700
Wavelength (nm)
g
Experiment
Simulation
200 µm
blue on
red on
both on
lateral LEDs
h
5 mm
i
1 cm

Figure 1. Wirelessly operated, dual-color microscale LED (micro-LED) probes for bidirectional, colocalized optogenetic control of neural activities. a, Schematic view of the probe inserted into the target brain area to perform dual-color neural activation and inhibition. **b**, Schematic, cellular scale depiction of the modulation function: red light regulates the cation channel ChrimsonR for depolarization, while blue light regulates the anion channel stGtACR2 for hyperpolarization. **c**, Exploded view of the dual-color LED probe made from vertically stacked blue and red thin-film micro-LEDs assembled on a flexible polyimide (PI) substrate, with a thin-film filter interface for spectrally selective reflection and transmission. **d**, Cross-sectional scanning electron microscopic (SEM) image of the probe structure, with false colors highlighting (from bottom to top) the indium gallium arsenide (InGaP) red micro-LED, the multilayer silicon dioxide / titanium dioxide (SiO_2/TiO_2) filter, and the indium gallium nitride (InGaN) blue micro-LED. Layers of SU-8 photoresists serve as the bonding materials. **e**, Optical images of a micro-LED probe (with a thickness of ~120 μm and a width of ~320 μm), showing independent control of blue and red emissions under current injections. **f**, Emission spectra of the blue and red micro-LEDs, in comparison with the action spectra of ion channels stGtACR2 and ChrimsonR (data extracted from references[7, 8]). **g**, Experimental photographs and simulated results illustrating blue and red light propagations for a micro-LED probe embedded into a brain phantom. Results for a probe with laterally assemble blue and red LEDs are also presented, showing misplaced blue and red emissions. Iso-intensity lines show 10% of the maximum power. **h**, Images of a micro-LED probe integrated with a wireless circuit for independent control of dual-color emissions. **i**, Photos of a behaving mouse after intracranial implantation of a probe, with (bottom) and without (top) the wireless circuit module.

Figure 2

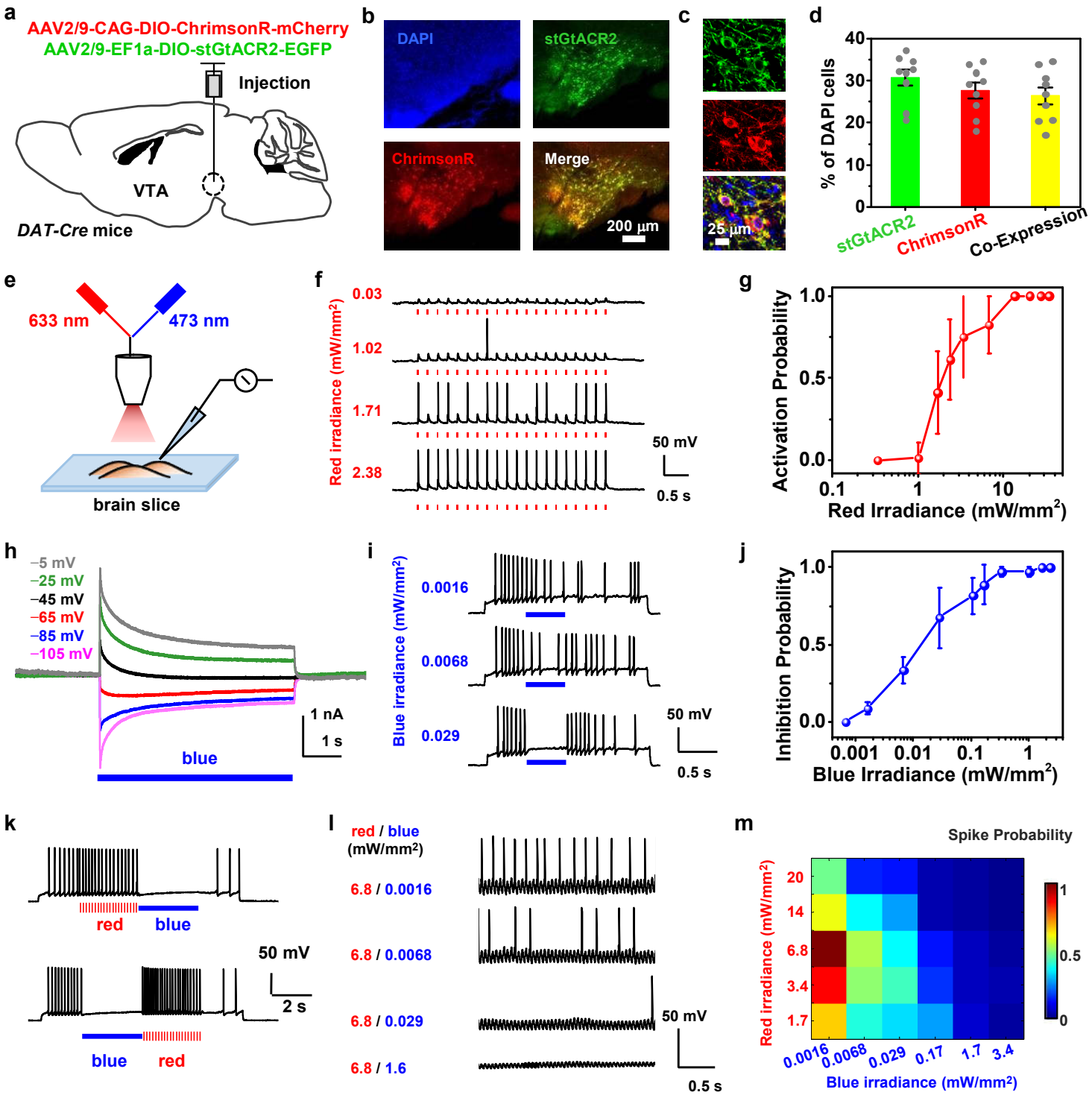
a
AAV2/9-CAG-DIO-ChrimsonR-mCherry
AAV2/9-EF1a-DIO-stGtACR2-EGFP
Injection
VTA
DAT-Cre mice
b
DAPI
stGtACR2
ChrimsonR
Merge
200 µm
c
25 µm
d
% of DAPI cells
40
30
20
10
0
stGtACR2
ChrimsonR
Co-Expression
e
633 nm
473 nm
brain slice
f
Red irradiance (mW/mm²)
0.03
1.02
1.71
2.38
50 mV
0.5 s
g
Activation Probability
1.0
0.5
0.0
0.1
1
10
Red Irradiance (mW/mm²)
h
−5 mV
−25 mV
−45 mV
−65 mV
−85 mV
−105 mV
1 nA
1 s
blue
i
Blue irradiance (mW/mm²)
0.0016
0.0068
0.029
50 mV
0.5 s
j
Inhibition Probability
1.0
0.5
0.0
0.001
0.01
0.1
1
Blue Irradiance (mW/mm²)
k
red
blue
50 mV
2 s
blue
red
l
red / blue
(mW/mm²)
6.8 / 0.0016
6.8 / 0.0068
6.8 / 0.029
6.8 / 1.6
50 mV
0.5 s
m
Spike Probability
Red irradiance (mW/mm²)
20
14
6.8
3.4
1.7
0.0016
0.0068
0.029
0.17
1.7
3.4
Blue irradiance (mW/mm²)
1
0.5
0

Figure 2. Bidirectional optogenetic activation and inhibition of neurons with red and blue light stimulation. a, Schematic strategy for co-expressing ChrimsonR and stGtACR2 in the ventral tegmental area (VTA) of *DAT-cre* mice. **b**, Immunostained fluorescence images of the VTA region expressing DAPI (blue), stGtACR2 (green), and ChrimsonR (red) and a merged image, 3 weeks after viral injection. **c**, Zoomed view showing cells co-expressing stGtACR2 (green) and ChrimsonR (red). **d**, Percentages of stGtACR2-, ChrimsonR- and co-expressing neurons among DAPI cells in the VTA (mean ± s.e.m., 3 slices per animal, $n = 3$ mice). **e**, Illustration of the experiment setup with combined blue (480 nm) and red (633 nm) laser beams (spot diameter ~1 mm) for optogenetic stimulating brain slices during patch-clamp recordings *in vitro*. **f**, Example traces showing neural activation by pulsed red light at different irradiances (20 Hz, 10-ms pulse, 20-pulse train). **g**, Activated spike probability as a function of red irradiances (mean ± s.e.m., $n = 4$ cells). **h**, Example photocurrents of neurons at membrane potentials varied from −105 mV to −5 mV (bottom to top), under continuous blue light illumination (duration 5 s, irradiance 8 mW/mm^2). **i**, Example traces of neural inhibition by continuous blue light at different irradiances (duration 0.5 s). **j**, Inhibited spike probability as a function of blue irradiances (mean ± s.e.m., $n = 5$ cells). **k**, Traces presenting bidirectional spike activation and inhibition with alternating red and blue illuminations (Patching current +90 pA; Red: duration 3 s, 20 Hz, 10-ms pulse, 2.2 mW/mm^2; Blue: duration 3 s, 8.5 mW/mm^2). **l**, Example traces of neural activities with simultaneous red and blue illuminations at different irradiances (duration 6 s). **m**, Summarized plot of measured spike probability (normalized mean values) as a function of red and blue irradiances ($n = 5$ cells).

Figure 3

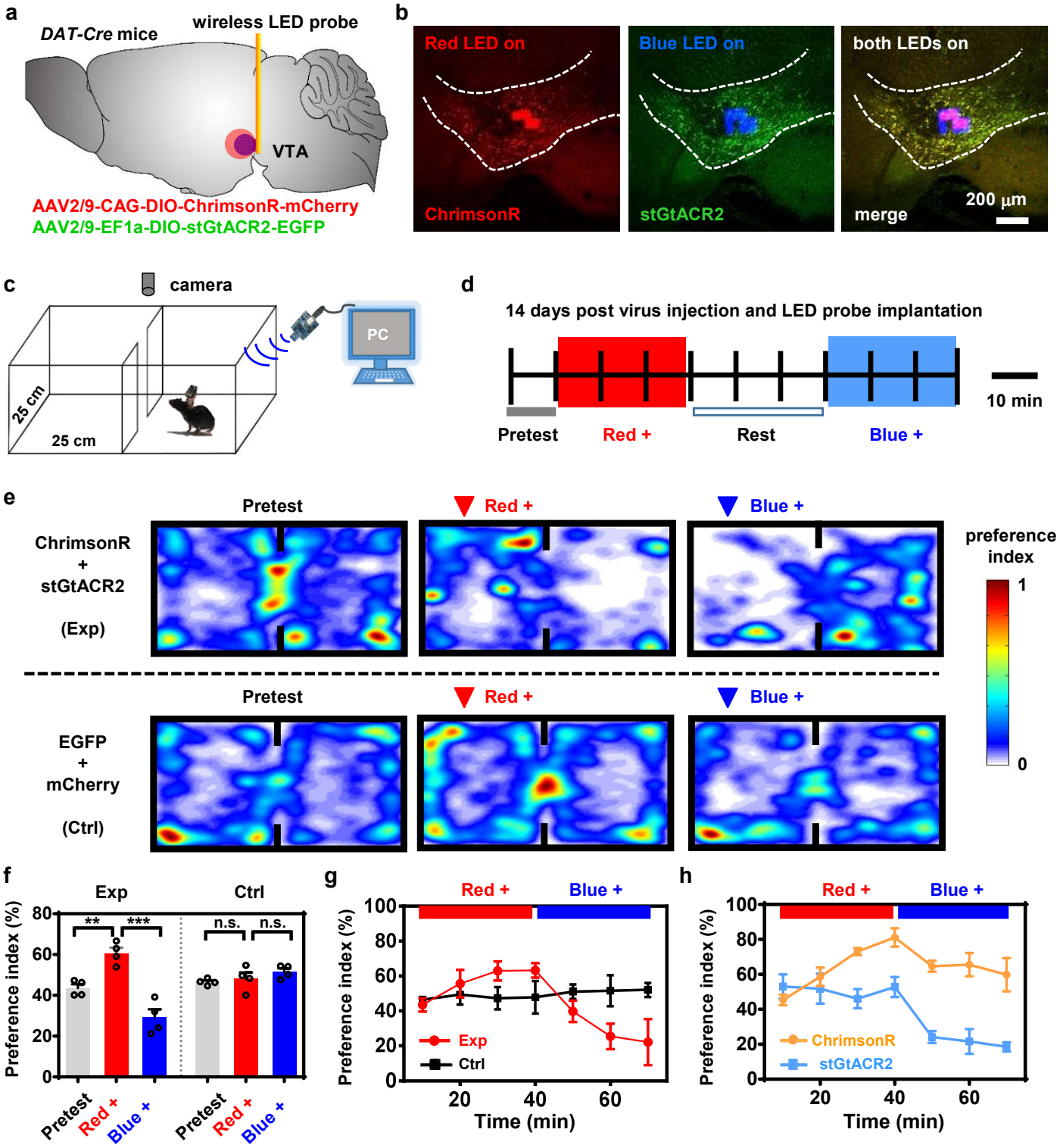
a
DAT-Cre mice
wireless LED probe
VTA
AAV2/9-CAG-DIO-ChrimsonR-mCherry
AAV2/9-EF1a-DIO-stGtACR2-EGFP
b
Red LED on
ChrimsonR
Blue LED on
stGtACR2
both LEDs on
merge
200 μm
c
camera
PC
25 cm
25 cm
d
14 days post virus injection and LED probe implantation
10 min
Pretest
Red +
Rest
Blue +
e
Pretest
Red +
Blue +
ChrimsonR
+
stGtACR2
(Exp)
EGFP
+
mCherry
(Ctrl)
preference
index
1
0
f
Exp
Ctrl
Preference index (%)
**
***
n.s.
n.s.
Pretest
Red +
Blue +
g
Red +
Blue +
Preference index (%)
Exp
Ctrl
Time (min)
h
Red +
Blue +
Preference index (%)
ChrimsonR
stGtACR2
Time (min)

Figure 3. Bidirectional, *in vivo* optogenetic regulation of animals' preference or aversion behaviors with wirelessly operated, dual-color microscale LED (micro-LED) probes. a, Diagram illustrating the combined viral injection (AAV2/9-CAG-DIO-ChrimsonR-mCherry and AAV2/9-EF1a-DIO-stGtACR2-EGFP) followed by implanting the micro-LED probe into the VTA of *DAT-cre* mice. **b**, Micrographs of the VTA showing co-expression of stGtACR2 and ChrimsonR, with a dual-color micro-LED probe embedded into the tissue. **c**, Illustration of the real-time place preference test with a two-compartment arena, where a mouse receives signals for dual-color control and its locomotion is recorded by a camera. **d**, Patterns used for optogenetic modulations, including a 10-min pretest, a 30-min red LED stimulation (20 Hz, 10-ms pulse, current 7 mA), a 30-min rest, and a 30-min blue LED stimulation (continuous, current 5 mA). **e**, Representative heat maps showing real-time preference and aversion behavior following red or blue stimulation for mice co-expressing stGtACR2 + ChrimsonR (experiment, or Exp) or EGFP + mCherry (control, or Ctrl). **f**, Summary of preference indices (the ratio of the time that mice spend in the left chamber to the whole recorded time) under red and blue stimulations for Exp and Ctrl groups (n = 4 mice each). Student's t test, ** $P < 0.01$, *** $P < 0.001$, n.s. $P > 0.1$. **g**, Preference indices measured at different times under red and blue stimulations for Exp and Ctrl groups (n = 4 mice each). **h**, Preference indices measured at different times under red and blue stimulations for groups expressing only ChrimsonR or stGtACR2 (n = 3 mice each).

Figure 4

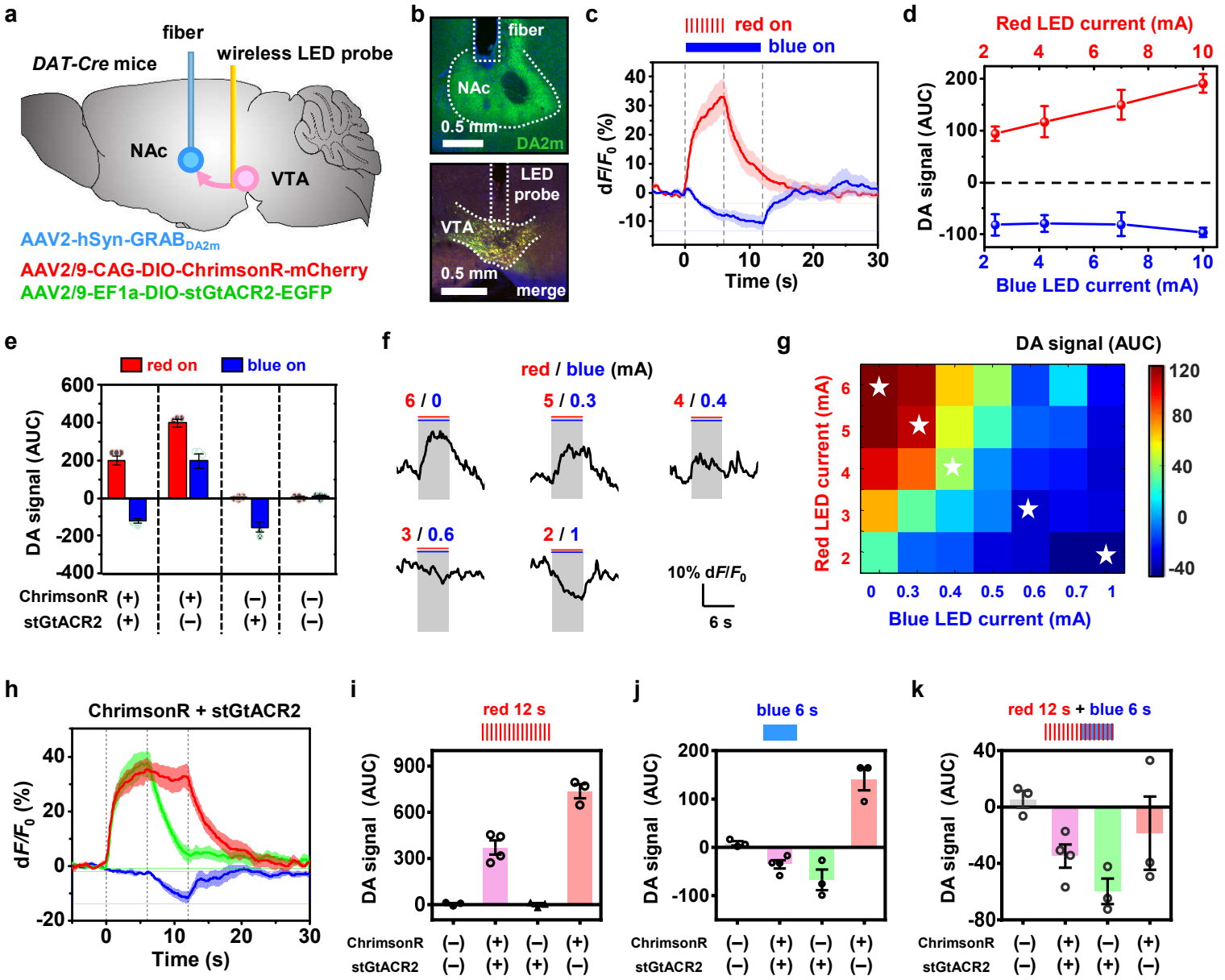
a
fiber
wireless LED probe
DAT-Cre mice
NAc
VTA
AAV2-hSyn-GRAB$_{DA2m}$
AAV2/9-CAG-DIO-ChrimsonR-mCherry
AAV2/9-EF1a-DIO-stGtACR2-EGFP
b
fiber
NAc
0.5 mm
DA2m
LED probe
VTA
0.5 mm
merge
c
red on
blue on
dF/F0 (%)
Time (s)
d
Red LED current (mA)
DA signal (AUC)
Blue LED current (mA)
e
red on
blue on
DA signal (AUC)
ChrimsonR (+) (+) (–) (–)
stGtACR2 (+) (–) (+) (–)
f
red / blue (mA)
6 / 0
5 / 0.3
4 / 0.4
3 / 0.6
2 / 1
10% dF/F0
6 s
g
DA signal (AUC)
Red LED current (mA)
Blue LED current (mA)
h
ChrimsonR + stGtACR2
dF/F0 (%)
Time (s)
i
red 12 s
DA signal (AUC)
ChrimsonR (–) (+) (–) (+)
stGtACR2 (–) (+) (+) (–)
j
blue 6 s
DA signal (AUC)
ChrimsonR (–) (+) (–) (+)
stGtACR2 (–) (+) (+) (–)
k
red 12 s + blue 6 s
DA signal (AUC)
ChrimsonR (–) (+) (–) (+)
stGtACR2 (–) (+) (+) (–)

Figure 4. Bidirectional, *in vivo* optogenetic control of dopamine (DA) release simultaneously recorded in the nucleus accumbens (NAc) during dual-color stimulation in the VTA. a, Diagram illustrating the combined viral injection (AAV2/9-CAG-DIO-ChrimsonR-mCherry and AAV2/9-EF1a-DIO-stGtACR2-EGFP) followed by implanting the micro-LED probe into the VTA, and the viral injection (AAV2-hSyn-GRAB$_{DA2m}$) followed by optical fiber implantation into the NAc of *DAT-cre* mice. **b**, Micrographs of (top) the NAc showing expression of DA2m and the fiber track, (bottom) the VTA showing co-expression of stGtACR2 and ChrimsonR (merged color) and the micro-LED probe track, 2 weeks after viral injection and probe implantation. **c**, Representative traces of DA signal increase or decrease in response to stimulations by the red LED (7 mA, 20 Hz, 20-ms pulse, 6 s) or the blue LED (2.4 mA, continuous, 12 s). The solid lines and shaded areas indicate the mean and s.e.m., respectively (n = 4 mice). **d**, Accumulative DA signals in response to red and blue stimulations under different LED currents. AUC: area under the curve during stimulation. **e**, Summary of measured DA signals (AUC) under red or blue stimulations (Red LED: 20 Hz, 20-ms pulse, 10 mA, 6 s; Blue LED, continuous, 3 mA, 12 s) for different animal groups expressing: ChrimsonR + stGtACR2 (n = 4 mice), ChrimsonR + EGFP (n = 3 mice), stGtACR2 + mCherry (n = 3 mice), EGFP + mCherry (n = 3 mice). Student's t test. **f**, Example traces of DA signals under combined red and blue stimulations with varied LED currents. **g**, Summarized plot of measured DA signals (AUC) (mean value) as a function of red and blue LED currents for 6 s (n = 3 mice). **h**, Plots of optogenetically evoked DA transients for mice co-expressing stGtACR2 + ChrimsonR, in response to different stimulation patterns (Red: red LED on, 20 Hz, 20-ms pulse, 10 mA, 0–12 s; Blue: blue LED on, continuous, 3 mA, 6–12 s; Green: red LED on 0–12 s and blue LED on 6–12 s). The solid lines and shaded areas indicate the mean and s.e.m., respectively. (n = 4 mice). **i–k**, Summary of measured DA signals (AUC) for mice with and without stGtACR2 and ChrimsonR expressions (n = 3 or 4 mice each), in response to different stimulation patterns. **i**, red LED on, 20 Hz, 20-ms pulse, 10 mA, 0–12 s. **j**, blue LED on, continuous, 3 mA, 6–12 s. **k**, red LED on 0–12 s and blue LED on 6–12 s.

Figure S1

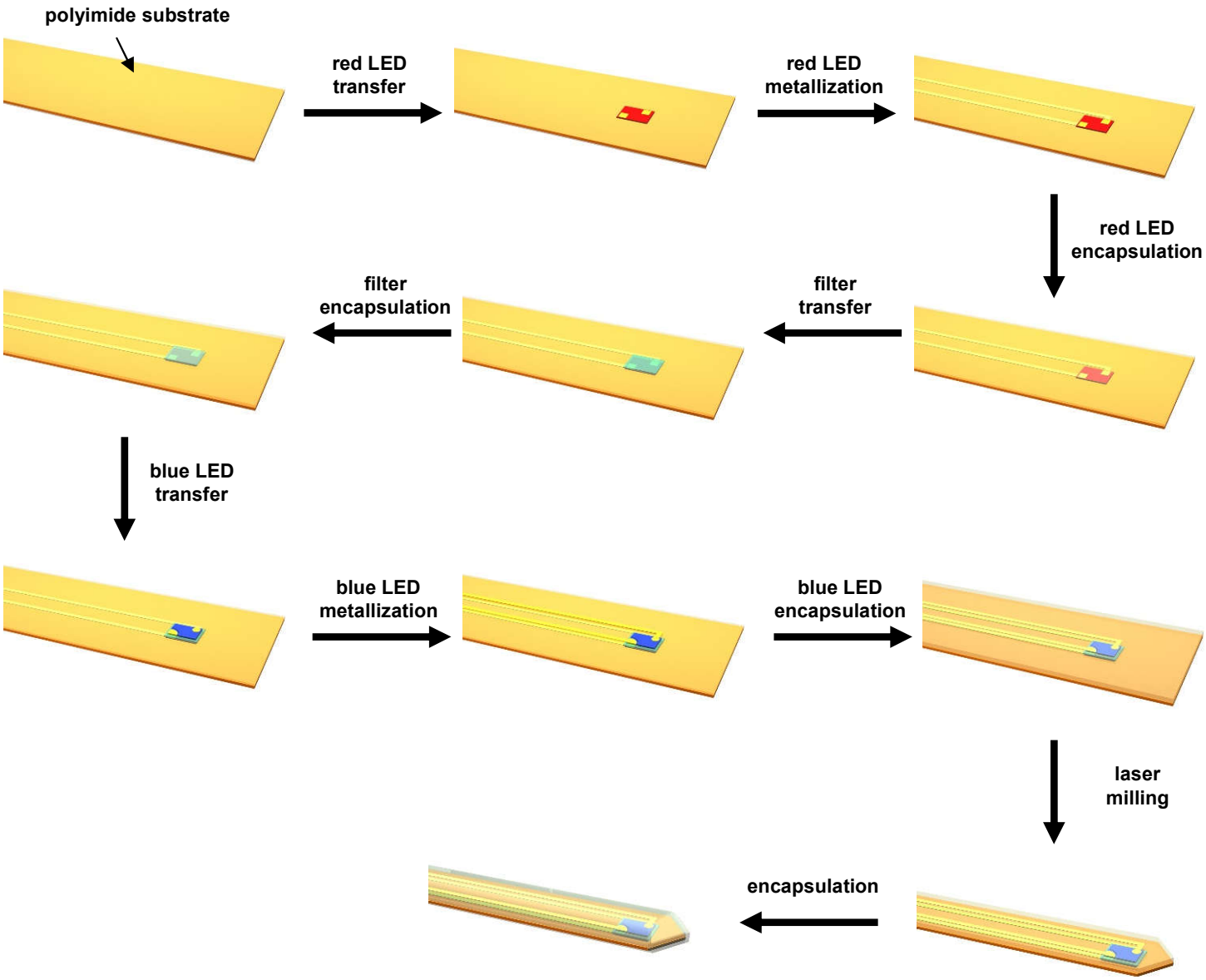

Figure S1. Schematic illustration of the process flow for fabricating the dual-color micro-LED probes, with vertically stacked red LED, filter and blue LED printed on PI substrates.

Figure S2

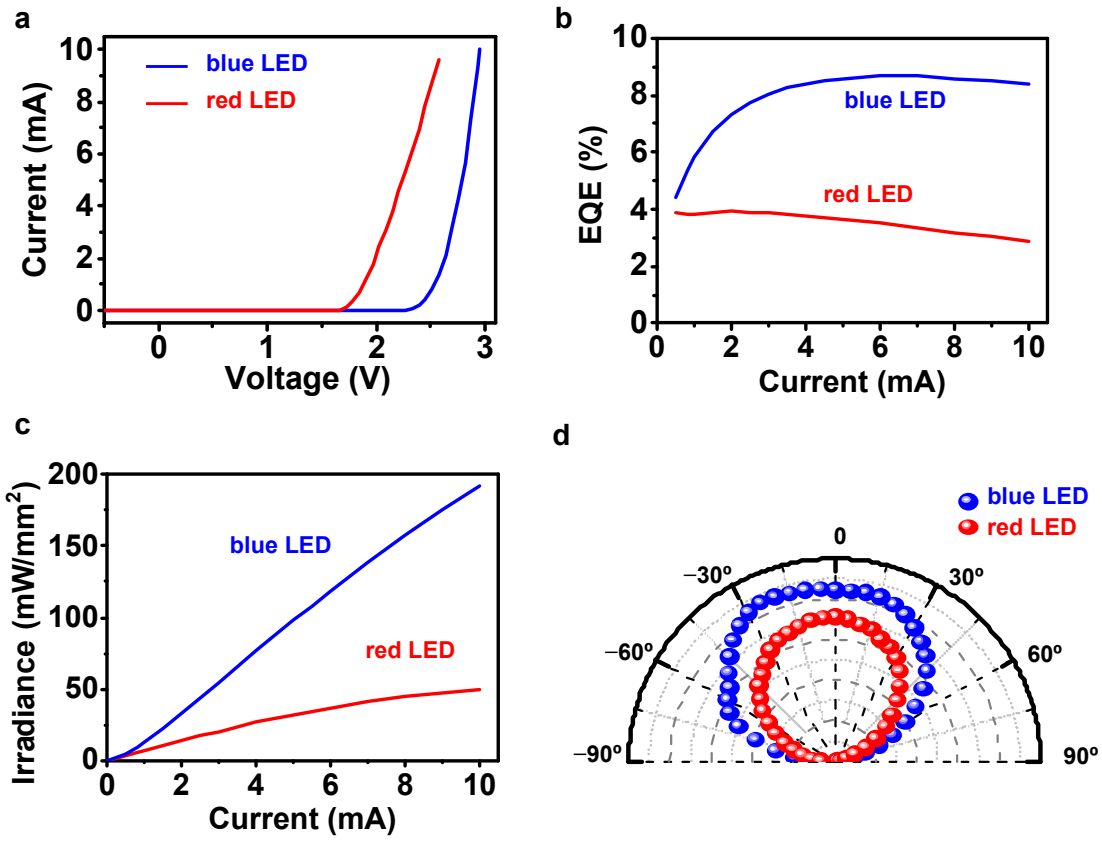

Figure S2. Measured optoelectronic properties of the red and the blue micro-LEDs in a probe structure. (a) Current–voltage curves. (b) External quantum efficiencies (EQEs) as a function of current. (c) Irradiance (power density on the LED surface) versus current. (d) Angular dependent emission profiles (in arbitrary unit).

Figure S3

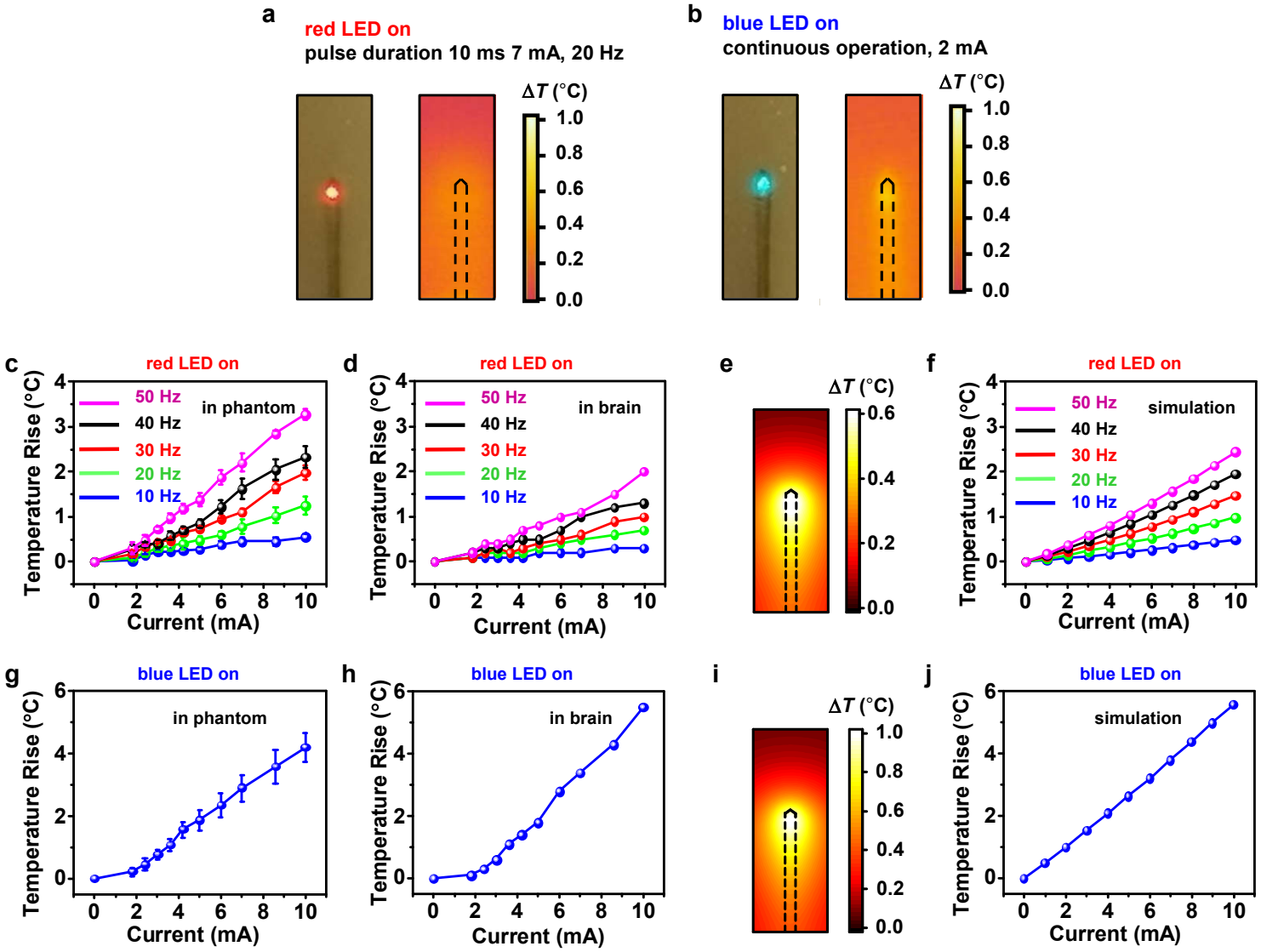

Figure S3. Thermal behaviors of a dual-color micro-LED probe. (a, b) Images and infrared thermographs showing a probe embedded into a brain phantom (~0.5 mm below the phantom surface). (a) Red LED on (injection current 7 mA, pulse frequency 20 Hz, pulse duration 10 ms). (b) Blue LED on (injection current 2 mA, continuous operation). (c–j) Measured and simulated temperature rise in phantom or brain when the red LED or the blue LED is on. (c) Temperature rise in phantom, measured by an infrared thermal camera when the red LED is on (current 0–10 mA, frequency 10–50 Hz, pulse duration 10 ms). (d) Temperature rise in the brain of living mice, measured with a thin wire thermocouple attached to the probe. (e) Simulated steady-state temperature distribution in the brain tissue surrounding the probe, when the red LED is on (current 7 mA, frequency 20 Hz, pulse duration 10 ms). (f) Simulated maximum temperature rise of the brain tissue when the red LED is in different operation conditions. (g–j) Corresponding results when the blue LED is on (continuous mode). current = 2 mA in (i).

Figure S4

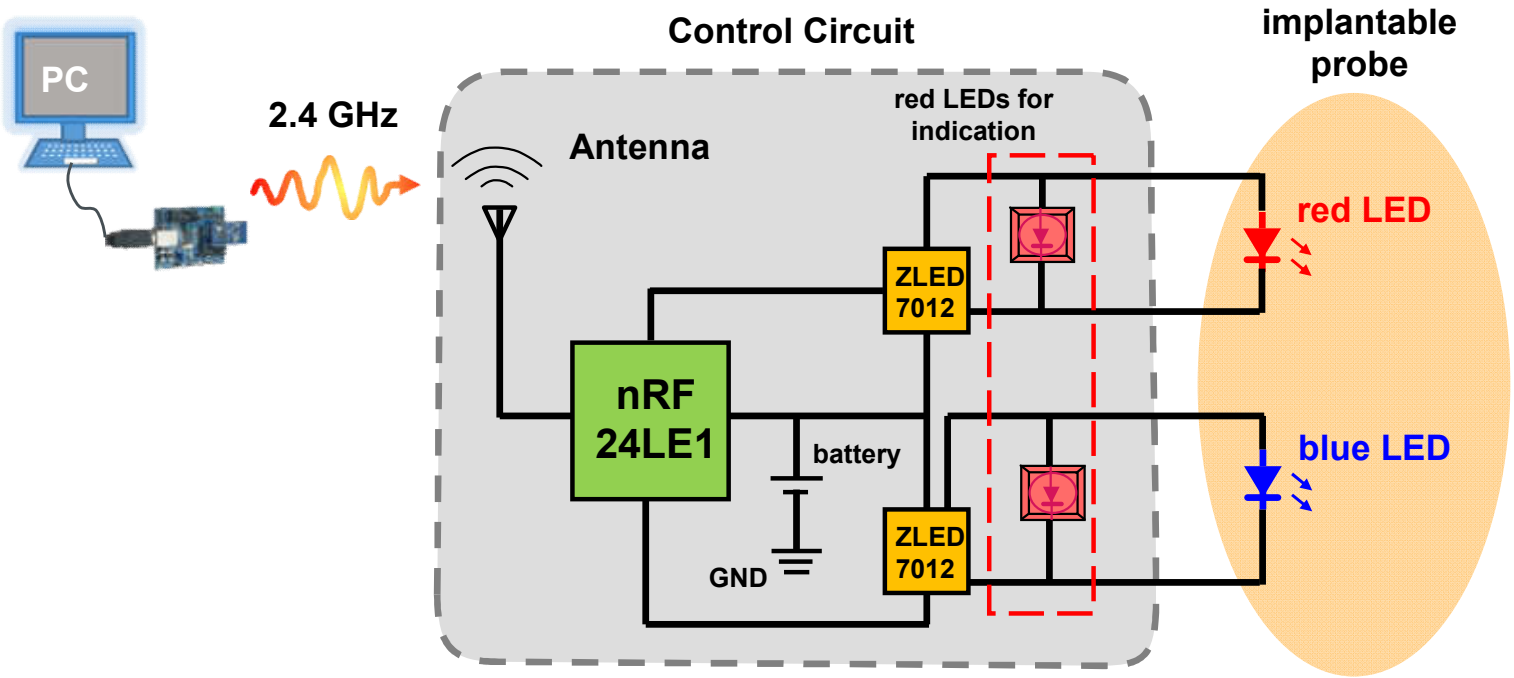

Figure S4. Schematic diagram showing the operational principle for the wireless circuit system controlling the dual-color micro-LED probe.

Figure S5

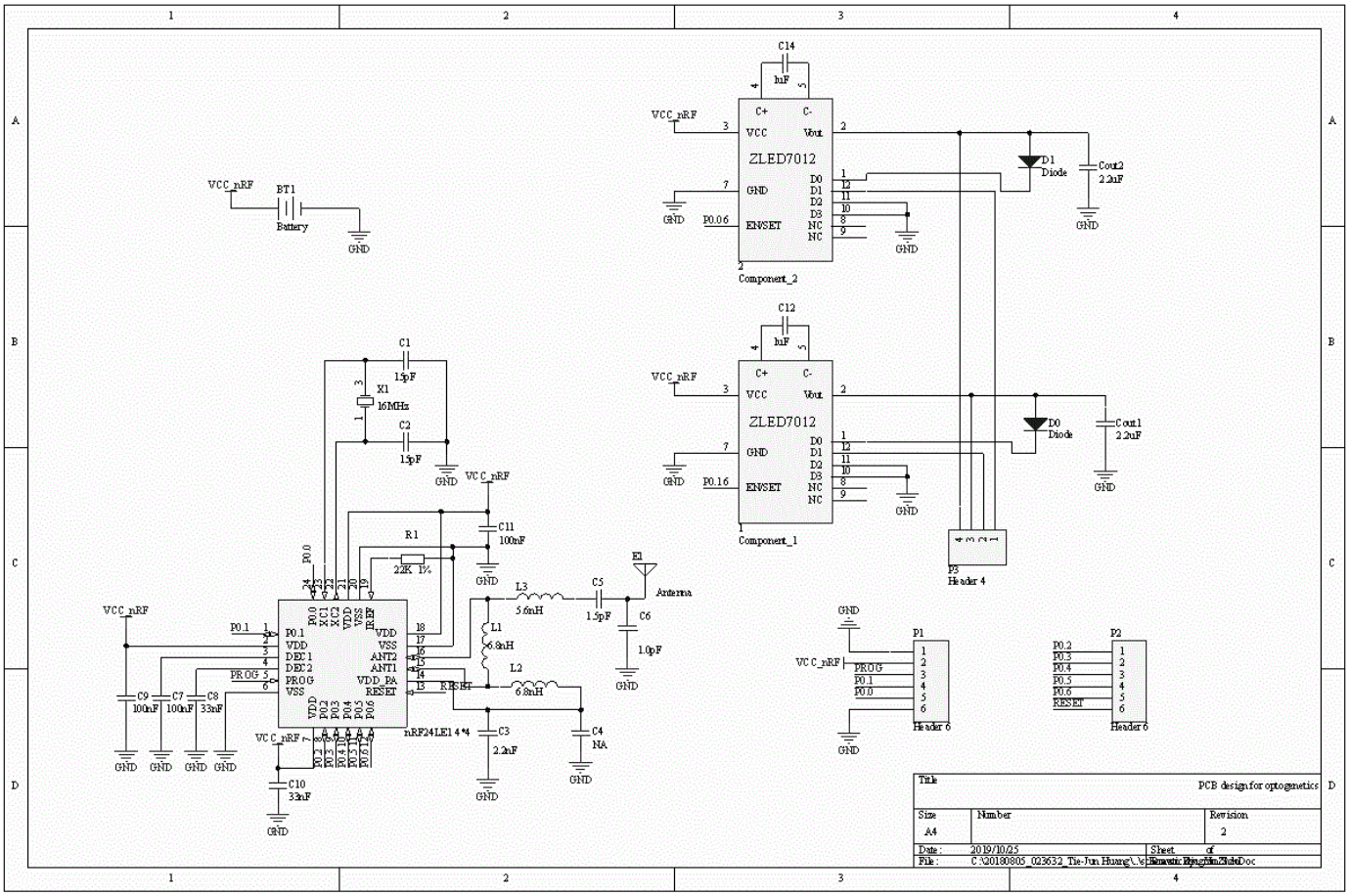

Figure S5. Detailed circuit design diagram of the wireless circuit system.

Figure S6

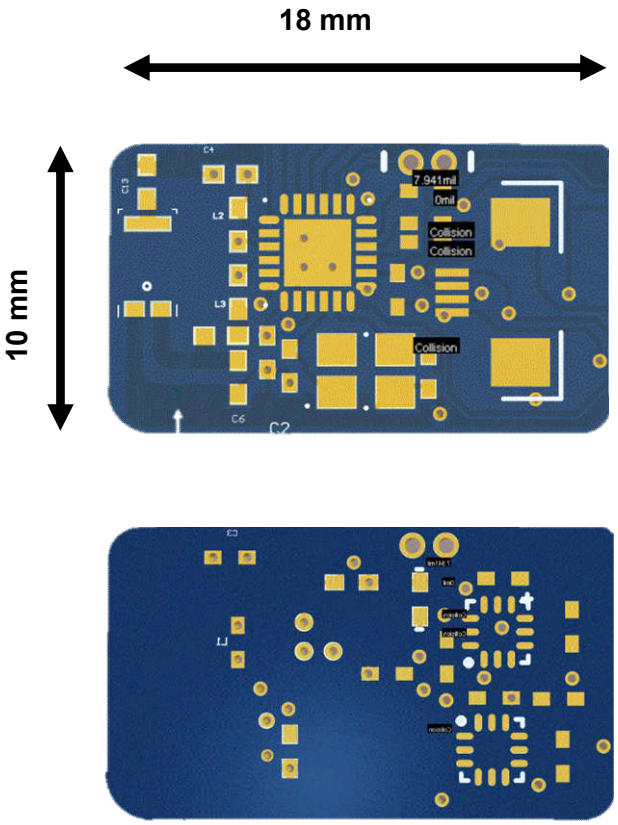

Figure S6. Layout of the designed printed circuit board (top: front view; bottom: back view).

Figure S7

	components
L1, L2	High frequency chip inductor +/- 5%, 6.8 nH
L3	High frequency chip inductor +/- 5%, 5.6 nH
C1, C2	NP0 +/- 2%, 15 pF
C3, C4	X7R +/- 10%, 2.2 nF
C5	NP0 +/- 0.1pF, 1.5 pF
C6	NP0 +/- 0.1pF, 1.0 pF
C7,C9,C11	X7R +/- 10%, 100 nF
C8,C10	X7R +/- 10%, 33 nF
C12,C14	X7R +/- 10%, 1 μF
Cout1,Cout2	2.2 μF
C13	NP0 50V, 10 pF
D0, D1	Indicating red LED, 610 nm, SMD 0402, 1 mm * 0.5 mm * 0.4 mm
R1	22 kΩ, 1%
nRF24LE1	nRF24LE1-F16Q24, QFN24 4 mm * 4 mm package, MCU
Component_1 Component_2	ZLED7012 ZI1R, LED current driver
X1	Crystal oscillator, SMD-3225, 16 MHz, CL=9 pF, +/- 60 ppm 3.2 mm * 2.5 mm package
E1	Antenna, H2U34WGTQW0100, AA055, 3.2 mm * 1.6 mm * 0.5 mm package
P1, P2	Pin Header, 6 pin, 1.25 mm, for programming
P3	FPC connector, 4 pin, 0.5 mm, for LED probe
P4	PCB header Connector, male, DIP Straight, 2 pin, 2.54 mm, for battery
Battery	Rechargeable lithium ion battery, 3.7 V, 45 mAh

Figure S7. List of components used in the wireless circuit system.

Figure S8

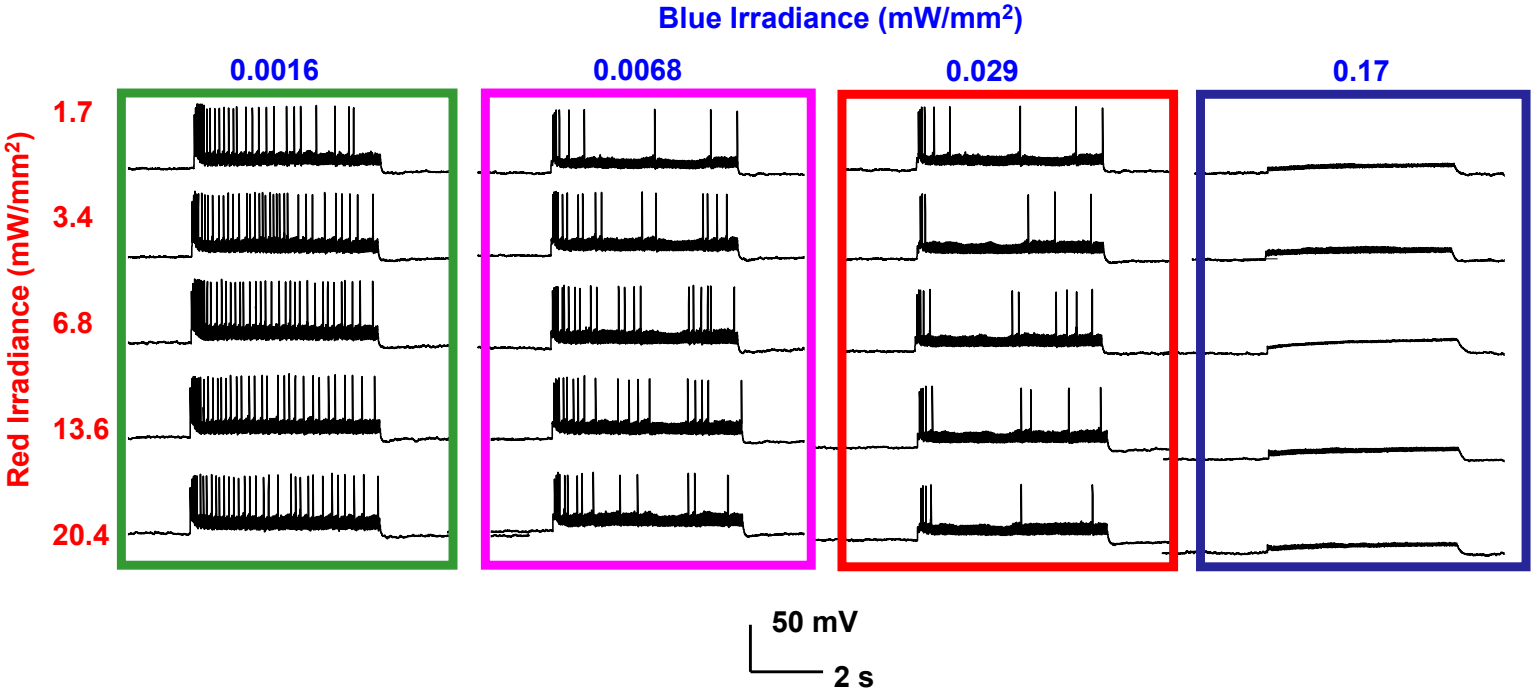

Figure S8. Recorded traces of a representative neuron with combined red and blue illumination at different irradiances. Red LED: 20 Hz, 10-ms pulse; Blue LED: continuous operation.

Figure S9

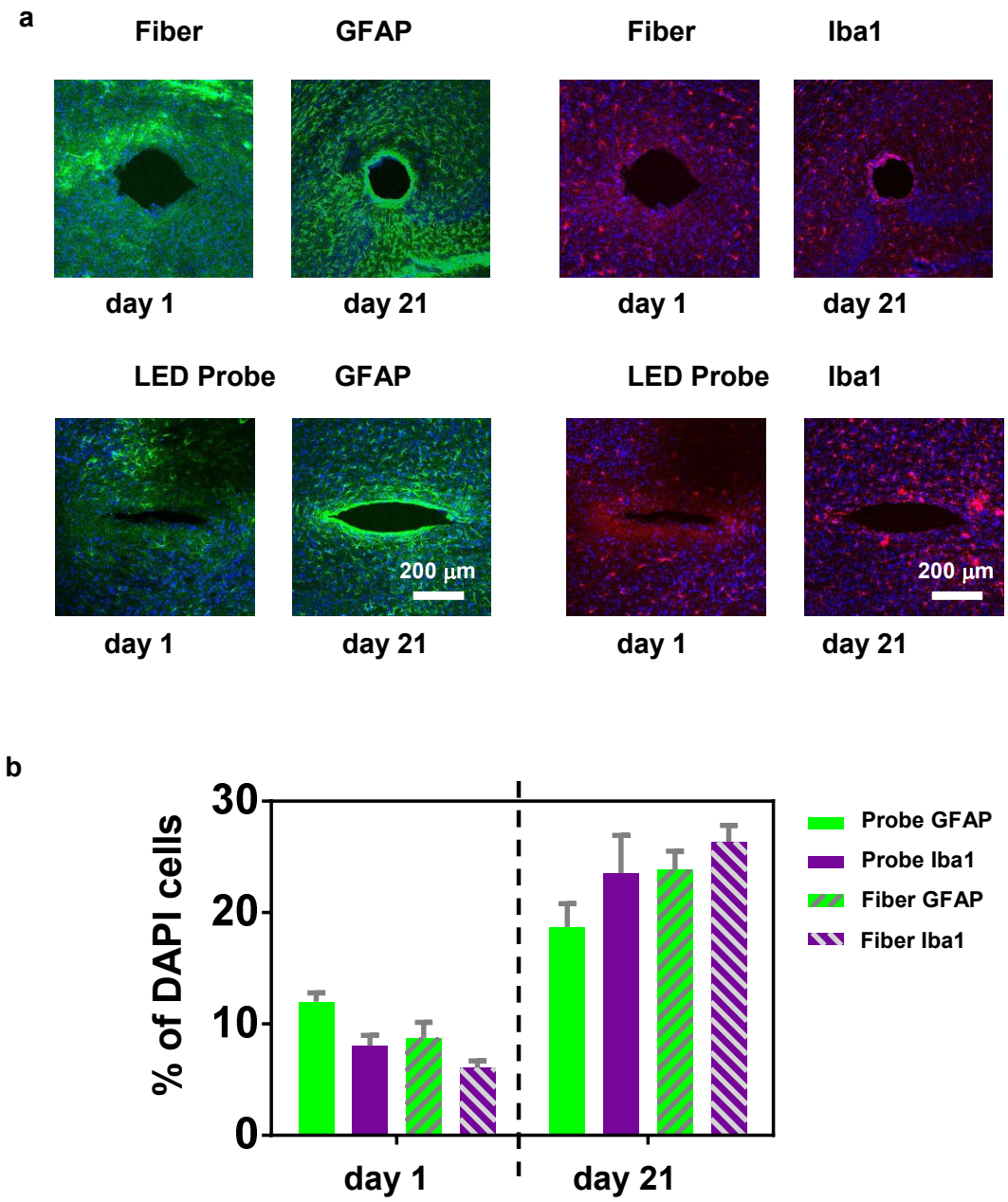

Figure S9. Immunoreactivity results showing the biocompatibility of the micro-LED probe, in comparison with those obtained with a silica based optical fiber. (a) Representative confocal fluorescence images of horizontal brain slices, showing immunohistochemical staining of astrocytes (GFAP) and activated microglia (Iba1) for both the LED probe and the fiber, after 1 day and 21 days implantation. Green: GFAP; Red: Iba1; Blue: DAPI. (b) Percentages of GFAP and Iba1 cell populations among DAPI cells collected at a distance of 200 µm from the edge of implantation. The LED probe and the fiber show similar results of inflammatory glial responses occurring after implantation. (n = 3 mice for each group).

Figure S10

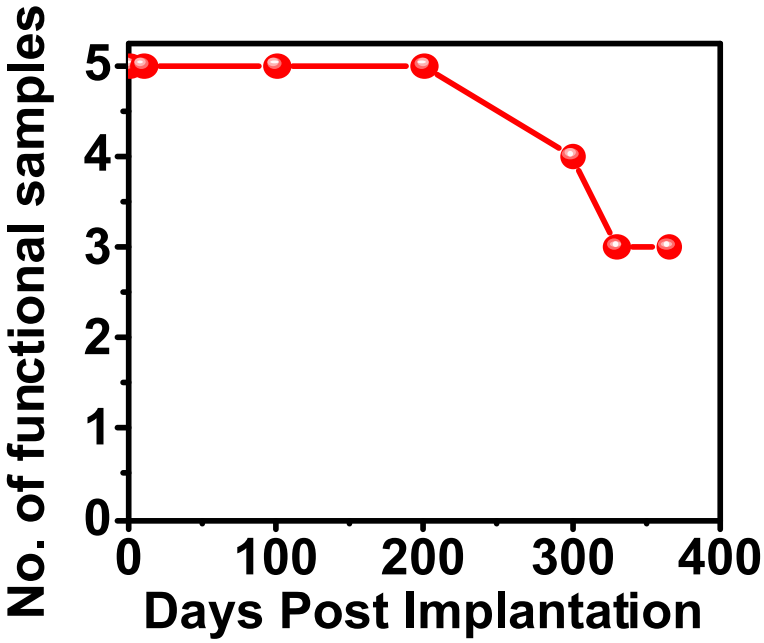

Figure S10. Number of functional micro-LEDs measured after chronic implantation in behaving mice.

Figure S11

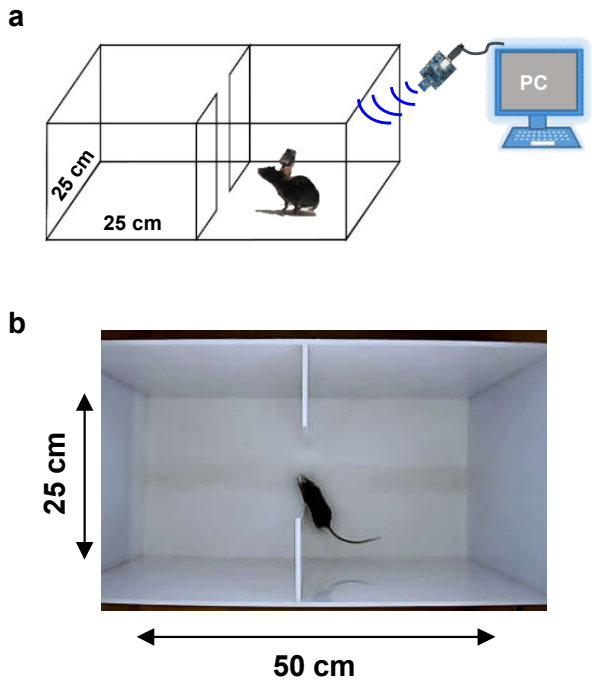

Figure S11. (a) Schematic diagram and (b) top-view photograph of the real-time place preference test with a two-compartment arena.

Figure S12

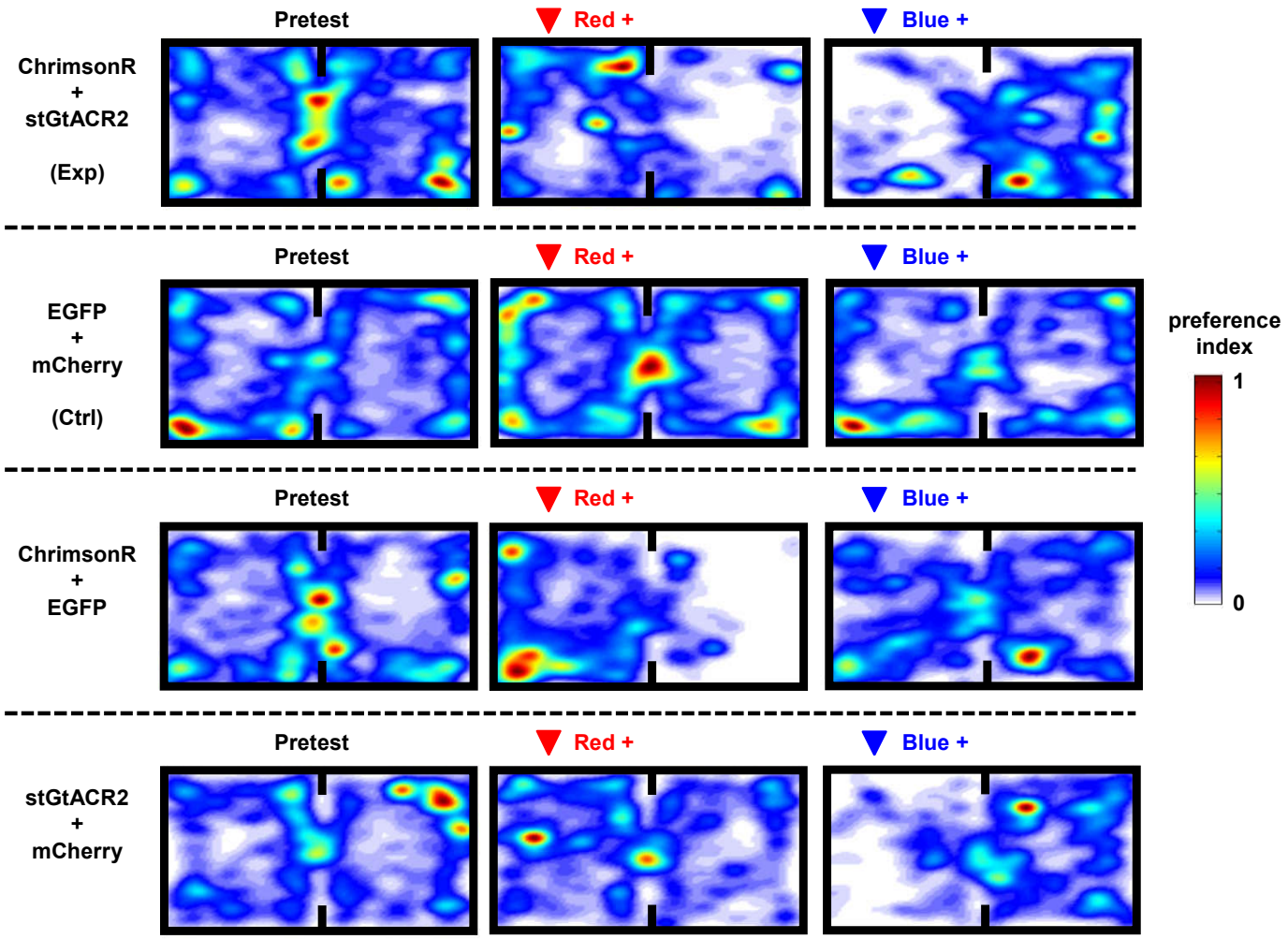

Figure S12. Representative heat maps showing real-time preference and aversion behavior following red or blue stimulation for mice expressing stGtACR2 + ChrimsonR (experiment, or Exp), EGFP + mCherry (control, or Ctrl), ChrimsonR + EGFP and stGtACR2 + mCherry. The data for ChrimsonR + stGtACR2 and EGFP + mCherry groups are identical to those presented in Fig. 3e.

Figure S13

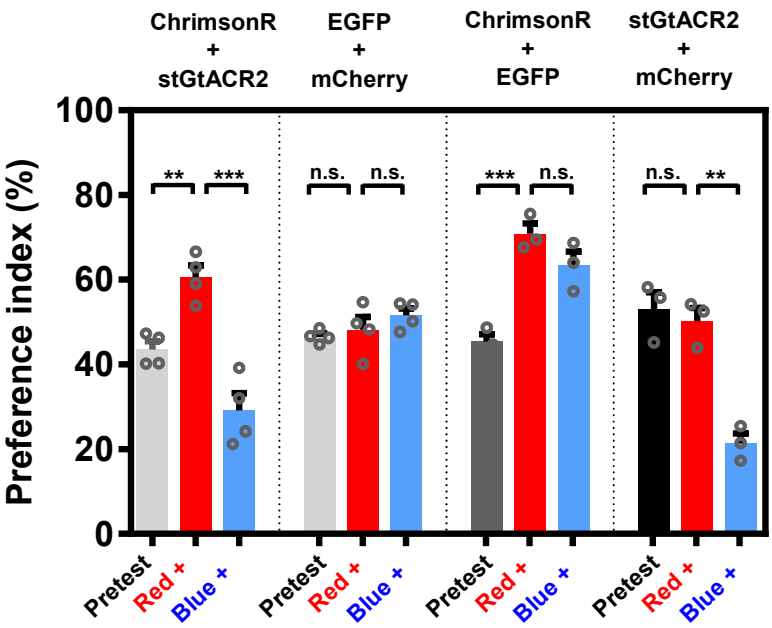

Figure S13. Summary of preference indices (the ratio of the time that mice spend in the left chamber to the whole recorded time) under red and blue stimulations for different animal groups expressing ChrimsonR + stGtACR2 (n = 4 mice), EGFP + mCherry (n = 4 mice), ChrimsonR + EGFP (n = 3 mice), stGtACR2 + mCherry (n = 3 mice). Student's t test, ** $P < 0.01$, *** $P < 0.001$, n.s. $P > 0.1$. The data for ChrimsonR + stGtACR2 and EGFP + mCherry groups are identical to those presented in Fig. 3f.

Figure S14

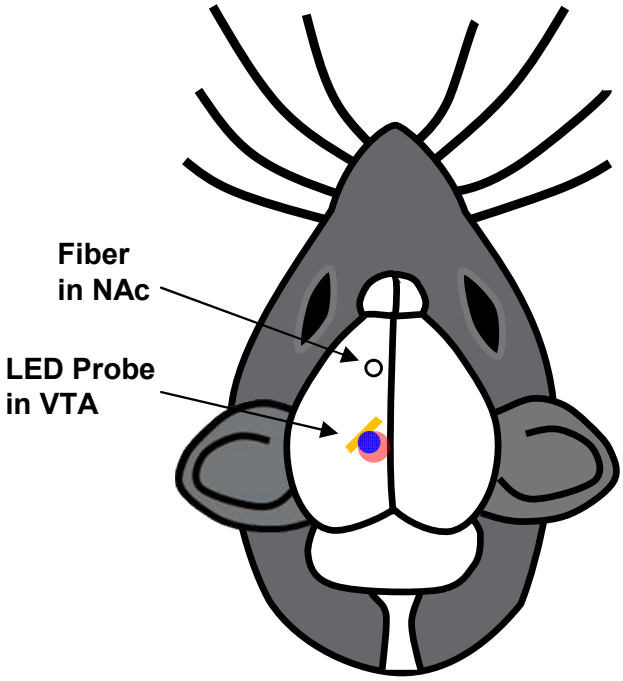

Figure S14. Schematic illustration (horizontal view) for the implantation of the fiber for DA recording in the NAc, and the dual-color LED probe for optogenetic stimulations in the VTA. The specific insertion angle is chosen for the LED probe, to minimize the optical crosstalk that disturbs the fiber photometric recording in the NAc.

Figure S15

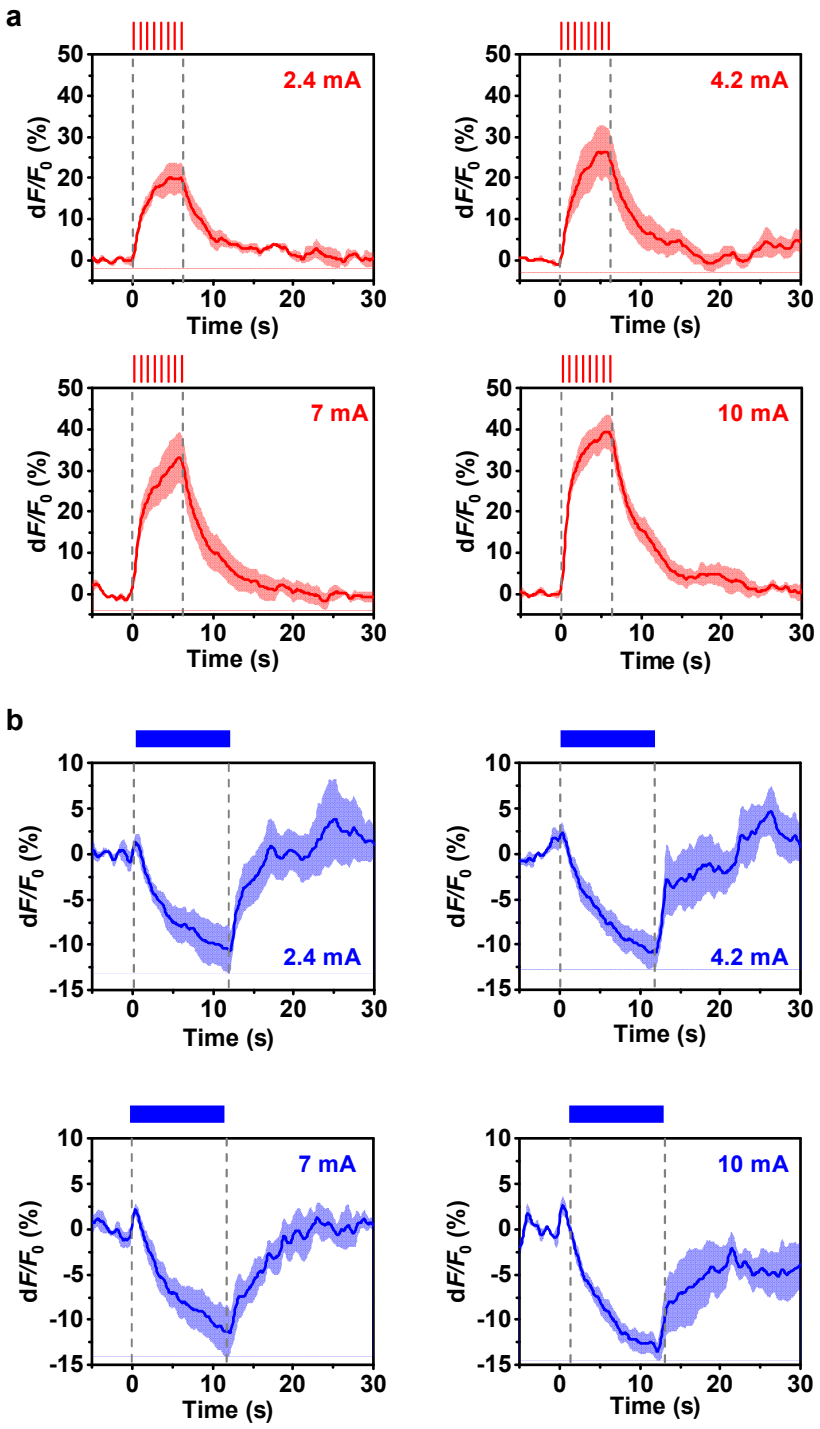

Figure S15. DA signals recorded as the fluorescence of $GRAB_{DA2m}$ in the NAc, in response to optogenetic stimulations applied in the VTA by red or blue micro-LEDs. (a, b) Representative traces of DA signals in response to stimulations by (a) the red LED (20 Hz, 20 ms, 6 s) and (b) the blue LED (continuous, 12 s) at various currents. The solid lines and shaded areas indicate the mean and s.e.m., respectively. (n = 4 mice). AUC: area under the curve during stimulation. The data for red LED at 7 mA and blue LED at 2.4 mA are identical to those presented in Figure 4c.

Figure S16

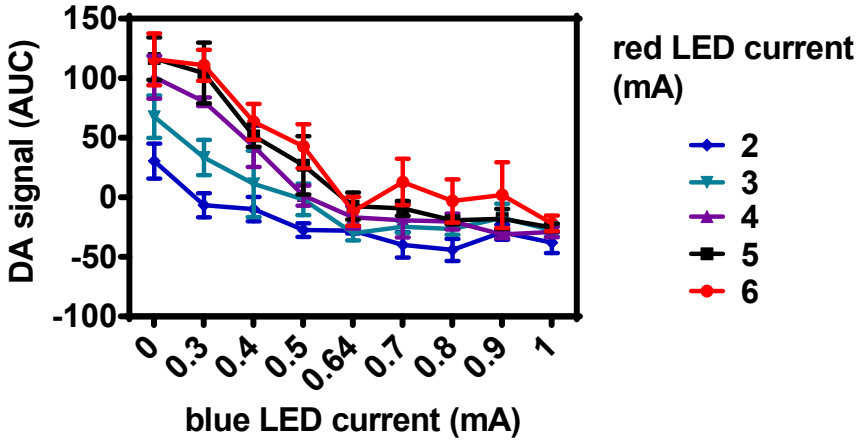

Figure S16. Detailed results of measured DA signals (AUC) with the combination of red and blue irradiance at different LED currents simultaneously for 6 s (n = 3 mice).

Figure S17

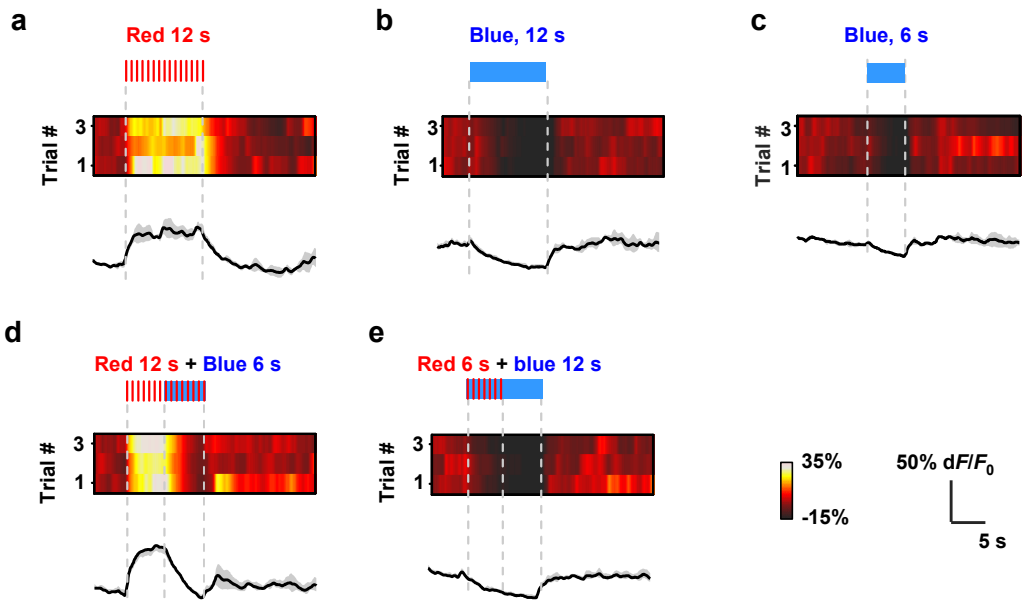

Figure S17. Example traces of optogenetically evoked DA transients for mice co-expressing stGtACR2 + ChrimsonR, in response to different stimulation patterns. (a) Red LED on, 20 Hz, 20-ms pulse, 10 mA, 0–12 s. (b) Blue LED on, continuous, 3 mA, 0–12 s. (c) Blue LED on, continuous, 3 mA, 6–12 s. (d) Red LED on 0–12 s and Blue LED on 6–12 s. (e) Red LED on 0–6 s and Blue LED on 0–12 s. The solid lines and shaded areas indicate the mean and s.e.m., respectively.

Figure S18

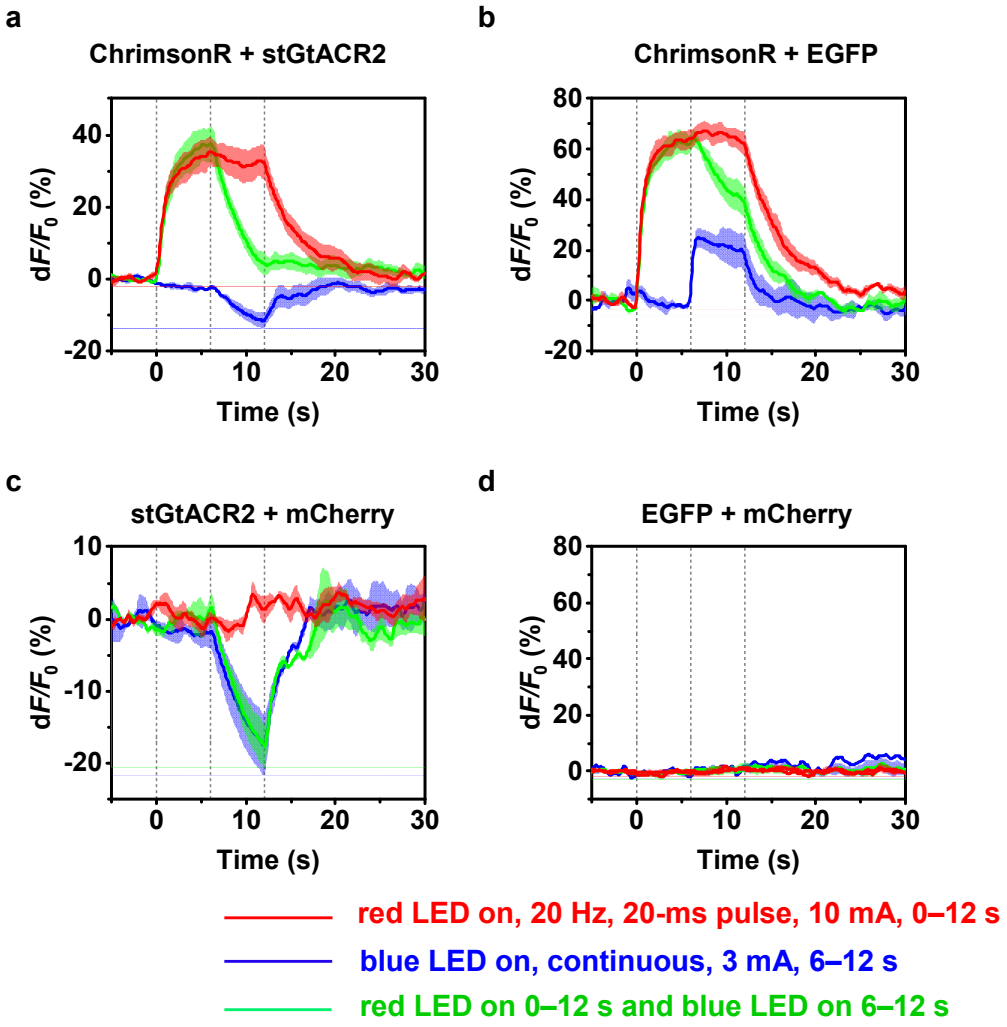

Figure S18. Plots of optogenetically evoked DA transients in response to different stimulation patterns (Red: red LED on, 20 Hz, 20-ms pulse, 10 mA, 0–12 s; Blue: blue LED on, continuous, 3 mA, 6–12 s; Green: red LED on 0–12 s and blue LED on 6–12 s), for different animal groups expressing (a) ChrimsonR + stGtACR2 (n = 4 mice), (b) ChrimsonR + EGFP (n = 3 mice), (c) stGtACR2 + mCherry (n = 3 mice), (d) EGFP + mCherry (n = 3 mice). The solid lines and shaded areas indicate the mean and s.e.m., respectively. The data in Figure S18a are identical to those presented in Figure 4h.

Movie S1

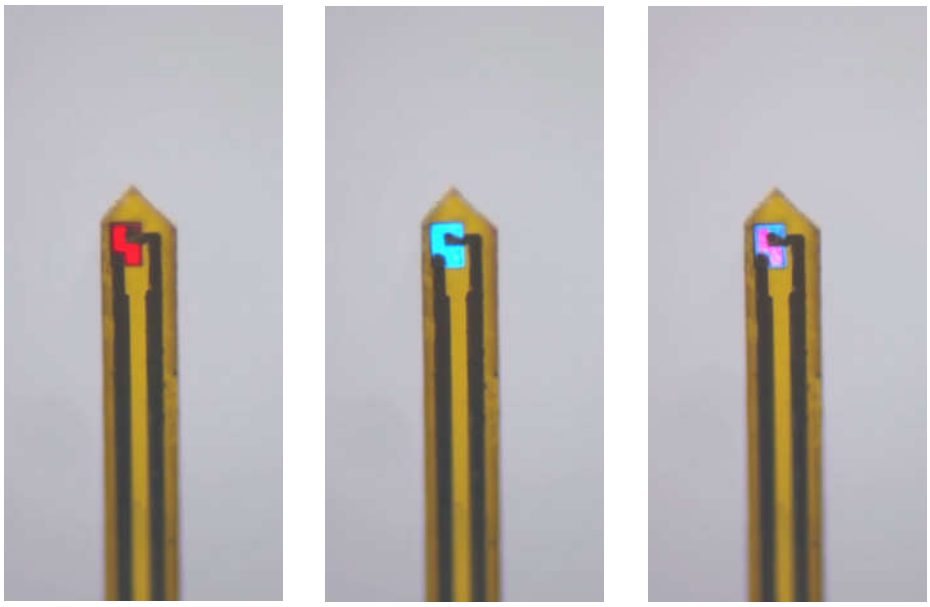

Movie S1. Video for dual-color micro-LED probe, displaying alternating blue and red emissions.

Movie S2

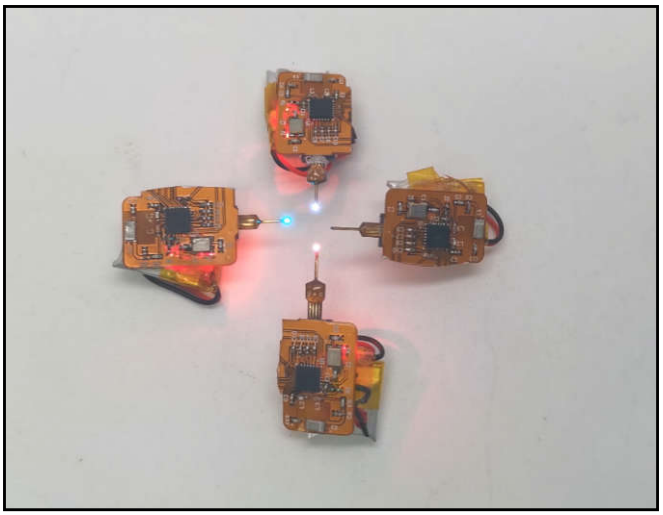

Movie S2. Video for multiple dual-color LED probes assembled with wirelessly operated circuit modules, showing capabilities for independent light emission control.

Movie S3

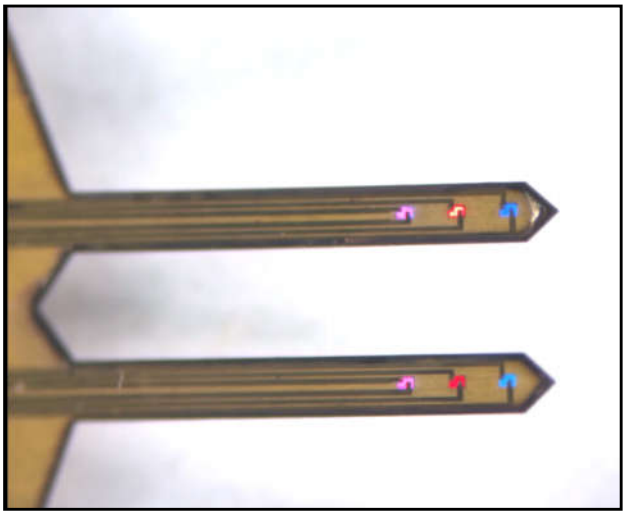

Movie S3. Video for multi-channel dual-color probes with 6 pairs of stacked red-blue micro-LEDs, displaying alternating blue and red emissions.

Movie S4

Movie S4. Video for four freely moving mice implanted with micro-LED probes and head-mounted circuits.

Movie S5

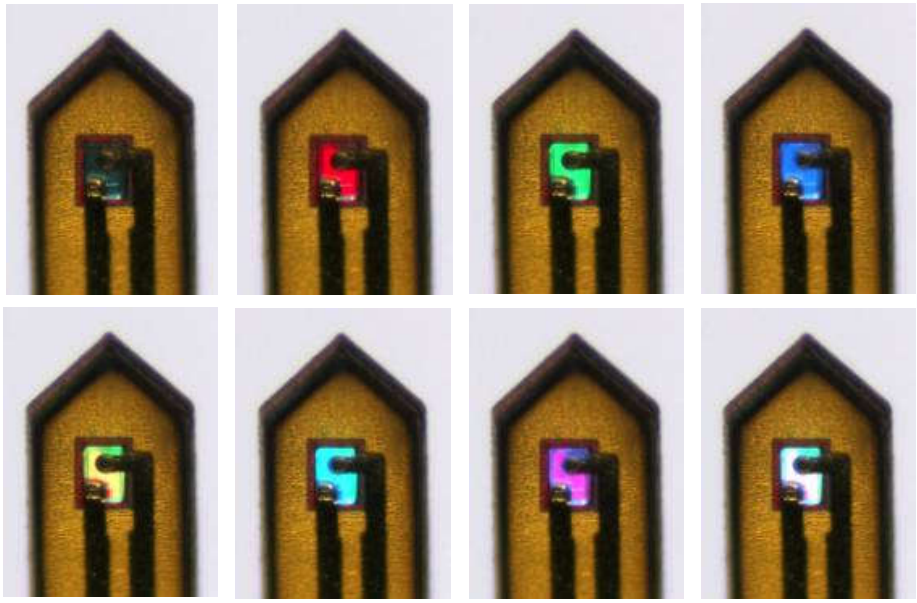

Movie S5. Video for a tri-color (red-green-blue) micro-LED needle structure, displaying different colors under current injection.

Supplementary Information

Device Fabrication

Fabrication of red and blue micro-LEDs

Details about the thin-film micro-LED structures and fabrication processes can be found in our previous work.[1,2] Via metal-organic chemical vapor deposition (MOCVD), red and blue LEDs are originally grown on gallium arsenide (GaAs) and sapphire substrates, respectively. The red LED active device contains an indium gallium phosphide (InGaP) based multiple quantum well structure (thickness ~5.6 μm) grown on GaAs with an $Al_{0.95}Ga_{0.05}As$ sacrificial interlayer. The blue LED active device contains an indium gallium nitride (InGaN) based multiple quantum well structure (thickness ~7 μm) grown on sapphire. Photolithographic process, wet / dry etching and metallic electrode deposition define the LED geometry (size ~ 180 μm × 125 μm). Freestanding, thin-film red LEDs are formed by selectively removing the $Al_{0.95}Ga_{0.05}As$ sacrificial layer in a hydrofluoric acid (HF) based solution. Freestanding, thin-film blue LEDs are formed by laser lift off (with a KrF excimer laser at 248 nm). Poly(dimethylsiloxane) (PDMS) based stamps are employed to pick up released thin-film micro-LEDs and transferred them onto other foreign substrates.

Fabrication of thin-film filters

Details about the thin-film filter fabrication can be found in our previous work.[3] The wavelength selective thin-film filters is based on a multilayered titanium dioxide

(TiO_2) and silicon dioxide (SiO_2) structure (thickness ~ 6.6 μm) comprising (from top to bottom): 19 nm TiO_2 / 15 periods (89 nm SiO_2 + 52 nm TiO_2) / 63 nm SiO_2 / 66 nm TiO_2 / 22 periods of (73 nm SiO_2 + 42.5 nm TiO_2) / 154 nm SiO_2. The structure is deposited on GaAs by ion beam-assisted sputter deposition. The filter shape (size ~ 180 μm × 125 μm) is defined by laser milling (Nd:YVO_4 laser, 1064 nm). After removing the GaAs substrate in solutions (NH_4OH:H_2O_2:H_2O = 1:1:2), freestanding thin-film filters can be picked up and transfer printed onto other foreign substrates by PDMS stamps.

Fabrication of dual-color micro-LED probes

The process flow to fabricate the dual-color micro-LED probe is described in Figure S1. The micro-LED probe is based on a flexible substrate made of composite polyimide (PI) and copper (Cu) films (from top to bottom: Cu/PI/Cu = 18/25/18 μm, from DuPont). From bottom to top, a red LED, an optical filter and a blue LED are sequentially transfer printed on the film by PDMS, in a vertical stack. Between each device layer, SU-8 based epoxy (thickness ~ 2–5 μm) serves an optically transparent and electrically insulating bonding layer. Each individual LED is metallized with sputtered metal layers (Cr/Au/Cu/Au = 10/100/500/100 nm). Laser milling (ultraviolet laser 365 nm) defines the needle shape (width ~ 320 μm, length ~ 5 mm). A bilayer of PDMS (~20 μm) and parylene (~15 μm) is used for waterproof encapsulation. For comparison in Fig. 1g, laterally arranged red-blue micro-LED probes are also fabricated with similar procedures.

Device Characterization and Modeling

Structural and optoelectronic characterizations

Scanning electron microscopic (SEM) images are taken with a ZEISS Auriga SEM / FIB Crossbeam System. Optical images are captured by a microscope MC-D800U(C). The LED emission spectra are measured with a spectrometer (HR2000+, Ocean Optics). Current–voltage characteristics are recorded by a Keithley 2400 source meter. LED irradiances and external quantum efficiencies are measured using a spectroradiometer with an integrating sphere (LabSphere Inc.). The angular dependent emission profiles are measured by a standard Si photodetector (DET36A, Thorlabs) with the device mounted on a goniometer. For *in vitro* test, micro-LED probes are implanted into the brain phantom. The brain phantom is made of agarose (0.5% w/v), hemoglobin (0.2% w/v), and intralipid (1% w/v) mixed in phosphate buffer solutions (98.3% w/v). After stirring, the mixed liquid is heated to boiling and then naturally cooled to room temperature, forming the gels.

Optical modeling

A ray tracing method based on Monte Carlo simulations is used to simulate the light propagation in the brain tissue. In the model, the tissue has absorption coefficients of 0.2 /mm and 0.08 /mm, and scattering coefficients of 47 /mm and 35 /mm, for blue (475 nm) and red (630 nm), respectively. The tissue has an anisotropy factor 0.85 and a refractive index of 1.36.[4]

Thermal characterizations

For *in vitro* experiments, the micro-LED probes are implanted into the brain phantom (~0.5 mm underneath the surface, at a depth of ~5 mm), and various currents are injected into the LEDs. The temperature distributions are mapped with an infrared camera (FOTRIC 228). For *in vivo* experiments, the micro-LED probe is bonded with an ultra fine flexible micro thermocouple (Physitemp, W-TW-44P/50) and inserted into the anesthetized mouse brain. Steady-state temperature rises are recorded from the thermocouple with a thermometer (Physitemp, BAT-12).

Thermal modeling

3D steady-state heat transfer models are established by finite element analysis (Comsol Multiphysics). The parameters of the brain use in the model include: density 1.1 g/cm^3, thermal conductivity 0.5 W/m/K, heat capacity 3650 J/kg/K, and the natural heat convection to air. The micro-LED probe serves as the heat source, with the input thermal power estimated by $P = V \times I \times (1 - \mathrm{EQE})$, where V, I and EQE are the measured voltage, current, and corresponding external quantum efficiencies for LEDs.

Wireless Circuit Design

A customized circuit module is designed to wirelessly operate the implantable micro-LED probe by independently controlling the red and the blue micro-LEDs for bi-directional modulation. The schematic diagram is depicted in Figure S4, with detailed circuit diagram, layouts and components presented in Figures S5, S6 and S7,

respectively. The core components include: a micro-controller (nRF24LE1, Nordic Semiconductor) operated at 2.4 GHz for data communication, and two LED drivers (ZLED7012, Renesas Electronics Corp.) with programmable current levels, frequencies, pulse widths for providing a constant current to micro-LEDs.[5] Two red LEDs are used on the circuit board outside the brain for signal indication, without affecting the mouse behaviors.[6] Control signals are wirelessly transmitted from the transmitting module connected to a laptop computer via an antenna operated at a radio frequency of 2.4 GHz, with a communication distance up to 50 m. The wireless circuit has a footprint of ~2.2 cm × 1.3 cm and a weight of 1.9 g (including a 0.9-g rechargeable lithium-ion battery with a capacity of 35 mAh). Used in the experimental conditions in this paper, the battery lifetime can reach up to 2 hours. The circuit can be connected with the implanted micro-LED probes via a flexible printed circuit (FPC) connector before animal experiment.

Biological Studies

Animals

Animal care is in accordance with the institutional guidelines of National Institute of Biological Sciences in Beijing (NIBS), with protocols proved by Institutional Animal Care and Use Committee (IACUC). All animals are socially housed in a 12 h/12 h (lights on at 8 am) light/dark cycle, with food and water *ad alibitum*. Wildtype C57BL6/N mice are purchased from VitalRiver (Beijing, China). *DAT-Cre* mice

106 (strain name B6.SJLSlc6a3tm1.1(cre) Bkmn; JAX Strain 006660) are at least six
107 weeks old at the time of surgery.

108 *Virus production*

109 The AAV2/9-CAG-DIO-ChrimsonR-tdTomato (Plasmid #130909) vector[7] is from
110 Addgene. The AAV2/9-EF1a-DIO-stGtACR2-EGFP-Kv2.1 plasmid is synthesized
111 and constructed according to the original reports.[8, 9] The AAV-hSyn-$GRAB_{DA2m}$
112 plasmid is provided by Prof. Yulong Li (Peking University).[10] AAV vectors are
113 packaged into serotype2/9 vectors, which consist of AAV2 ITR genomes pseudotyped
114 with AAV9 serotype capsid proteins. AAV vectors are replicated in HEK293 cells
115 with the triple plasmid transfection system and purified by chloroform,[11] resulting in
116 AAV vector titers of about 5×10^{12} particles/mL. Virus suspension is aliquoted and
117 stored at −80 °C. AAV titers are measured using real-time qPCR. Adeno-associated
118 viral particles are produced at the Vector Core Facility at Chinese Institute for Brain
119 Research, Beijing (CIBR).

120 *Stereotaxic Surgery*

121 Adult *DAT-Cre* mice are anesthetized with an intraperitoneal injection of Avertin (250
122 mg/kg) before surgery, and then placed in a mouse stereotaxic instrument. After
123 disinfection with 0.3% hydrogen peroxide, a small incision of the scalp is created to
124 expose the skull. Then, 0.3% hydrogen peroxide is applied to clean the skull. A small
125 craniotomy is made and a calibrated pulled-glass pipette (Sutter Instrument) is
126 lowered to the VTA (coordinates 3.64 mm posterior to the bregma, 0.5 mm lateral to
127 midline, and 4.6 mm ventral to the skull surface). Virus is delivered through a small

128 durotomy by a glass micropipette using a microsyringe pump (Nanoliter 2000 injector
129 with the Micro4 controller, WPI).

130 Four different combinations of virus are used for *in vivo* experiments:

131 1) ChrimsonR + stGtACR2 (AAV2/9-CAG-DIO-ChrimsonR-tdTomato and
132 AAV2/9-EF1a-DIO-stGtACR2-EGFP-Kv2.1, 1:1);

133 2) mCherry + EGFP (AAV2/9-EF1a-DIO-mCherry and AAV2/9-EF1a-DIO-EGFP,
134 1:1);

135 3) ChrimsonR + EGFP (AAV2/9-CAG-DIO-ChrimsonR-tdTomato and
136 AAV2/9-EF1a-DIO-EGFP, 1:1)

137 4) stGtACR2 + mCherry (AAV2/9-EF1a-DIO-stGtACR2-EGFP-Kv2.1 and
138 AAV2/9-EF1a-DIO-mCherry, 1:1)

139

140 A bolus of 0.4 μL of mixed virus is injected into the VTA at 46 nL/min. The pipette is
141 held in place for 10 min after the injection and then slowly withdrawn. For real-time
142 place preference (RTPP) behavioral test, the dual-color LED probe implantation is
143 carried out after virus injection and diffusion. The probe was slowly implanted at the
144 side of the target brain areas with an angle of 45° to midline (coordinates 3.64 mm
145 posterior to the bregma, 0.8 mm lateral to midline, and 4.85 mm ventral to the skull
146 surface). The probe is fixed to the skull with Cyanoacrylate adhesive (TONSAN
147 1454) and dental cement. For dopamine detection with fiber photometric recording,
148 the AAV-hSyn-GRAB$_{DA2m}$ (0.2 μL) is injected into the NAc (coordinates: 1.18 mm
149 front to the bregma, 0.75 mm lateral to midline, and 3.75 mm ventral to the skull

150 surface). Optical fiber implantation is carried out after virus injection and diffusion. A
151 piece of optical fiber (FT200UMT, 200 μm O.D., 0.39 NA, Thorlabs) is fit into an
152 LC-sized ceramic fiber ferrule (Shanghai Fiblaser, China) and implanted over the
153 target brain areas with the tip 0.1 mm above the virus injection sites in the NAc. The
154 ceramic ferrule is fixed to the skull with Cyanoacrylate adhesive (TONSAN 1454)
155 and dental cement. After the virus injection and device implantation, mice are housed
156 individually to prevent potential damage to the probe. All subsequent experiments are
157 performed at least 2 weeks after injection to allow sufficient time for transgene
158 expression and animal recovery.

159 *Immunohistochemistry*

160 The micro-LED probes are implanted into the VTA region and fixed to the skull with
161 Cyanoacrylate adhesive (TONSAN 1454) and dental cement. After 1 day or 3 weeks
162 following the surgery, animals are transcardially perfused with 4% PFA in 0.1 M PBS.
163 Brains are postfixed in 4% PFA and 40-μm-thick vibratome sections are prepared.
164 After 5-min PBS rinses for 3 times, the sections are blocked in PBST (PBS + 0.3%
165 Triton X-100) with 3% bovine serum albumin for 1 hour, and incubated in rabbit
166 anti-Iba1 (1:1000, Wako, Cat.#019-19741) and rabbit anti-GFAP antibody (1:2000,
167 Sigma, Cat#AB5541) dissolved in PBST at 4 °C for 24 hours. After 5-min washes in
168 PBS for 5 times, the sections are incubated with Alexa Cy3-conjugated goat
169 anti-rabbit antibody (1:500, Jackson ImmunoResearch) and Alexa 488 goat
170 anti-chicken antibody (1:500, Thermo Fisher Scientific) dissolved in PBST for 2
171 hours at room temperature followed by 5-min washes in PBS for 3 times. At last, the
172 samples are coverslipped in 50% glyceroland slides and photographed with an

173 automated slide scanner (VS120 Virtual Slide, Olympus) or a confocal scanning
174 microscope (DigitalEclipse A1, Nikon). The numbers of DAPI, stGtACR2 and
175 ChrimsonR stained cells or the numbers of Iba1+ microglia and GFAP+ astrocytes are
176 analyzed with Fiji software (https://fiji.sc/) and their percentages in cell population
177 indicated by DAPI are calculated.

178 *In vitro optogenetics evaluation*

179 Electrophysiological properties of the neurons in brain slices are measured with
180 whole-cell patch-clamp recording technique following a previously described
181 procedure.[12] After two weeks of virus expression (ChrimsonR + stGtACR2), mice are
182 deeply anesthetized with pentobarbital (100 mg/kg i.p.) and intracardially perfused
183 with 5 mL ice-cold oxygenated modified artificial cerebrospinal fluid (ACSF) at a rate
184 of 2 mL/min. After perfusion with modified ACSF containing (in mM): 225 sucrose,
185 119 NaCl, 2.5 KCl, 0.1 $CaCl_2$, 4.9 $MgCl_2$, 1.0 NaH_2PO_4, 26.2 $NaHCO_3$, 1.25 glucose,
186 3 kynurenic acid, and 1 Na L-ascorbate (Sigma-Aldrich), brains are quickly removed
187 and placed in ice-cold oxygenated ACSF containing (in mM): 110 choline chloride,
188 2.5 KCl, 0.5 $CaCl_2$, 7 $MgCl_2$, 1.3 NaH_2PO_4, 25 $NaHCO_3$, 20 glucose, 1.3 Na
189 ascorbate, and 0.6 Na pyruvate. Sagittal sections (200 μm thick) are prepared using a
190 Leica VT1200S vibratome. Brain slices are incubated for 1 hour at 34 °C with ACSF
191 saturated with 95% O_2/5% CO_2 and containing (in mM) 125 NaCl, 2.5 KCl, 2 $CaCl_2$,
192 1.3 $MgCl_2$, 1.3 NaH_2PO_4, 25 $NaHCO_3$, 10 glucose, 1.3 Na ascorbate, and 0.6 Na
193 pyruvate. The internal solution within whole-cell recording pipettes (3–6 MΩ)
194 contains (in mM): 130 K-gluconate, 10 HEPES, 0.6 EGTA, 5 KCl, 3 Na_2ATP, 0.3

195 Na_3GTP, 4 $MgCl_2$, and 10 Na_2-phosphocreatine (pH 7.2–7.4). Voltage-clamp
196 recordings are performed using a MultiClamp 700B amplifier (Molecular Devices).
197 Traces are low-pass filtered at 2.6 kHz and digitized at 10 kHz (DigiData 1440,
198 Molecular Devices). The data are acquired and analyzed using Clampfit 10.0 software
199 (Molecular Devices). Red and blue illuminations are provided by a fiber coupled to
200 two laser sources (wavelengths 633 nm and 473 nm).

201 *Real-time place preference test*

202 After 2 weeks of recovery and AAV expression in *DAT-cre* mice, real-time place
203 preference / avoidance (RTPP) tests are performed in a custom-made
204 two-compartment apparatus. The RTPPT apparatus comprises two white plastic
205 chambers (size: 25 × 25 × 30, L × W × H in cm), separated by a half-open opaque
206 plastic walls in the middle (8 × 30, L × H cm). A RTPP test consists of 3 phases:
207 10-min baseline (pretest), 30-min red LED stimulation, 30-min rest (no stimulation),
208 and 30-min blue LED simulation. During the pretest phase, individual mice are
209 allowed to freely explore the entire apparatus for 10 min. Animals that exhibit a
210 strong initial preference or avoidance for one of the side chambers (preference index >
211 60% or < 40%) are excluded from further experiments. During the red LED
212 stimulation phase, animals that entered the left chamber receive red light pulses (20
213 Hz, 20-ms pulse, 7 mA). During the blue light stimulation phase, animals that entered
214 the left chamber receive constant blue light (continuous, 5 mA). The locomotion of
215 animals is assessed from the video recording data using a custom-developed
216 MATLAB program.

217 *Fiber photometry for dopamine (DA) detection*

218 Details for the fiber photometric system are described previously.[13] The excitation
219 source is a 488 nm semiconductor laser (Coherent, Inc. OBIS 488 LS, tunable power
220 up to 60 mW). A dichroic mirror with a 452–490 nm reflection band and a 505–800
221 nm transmission band (Thorlabs, Inc. MD498) is employed for wavelength selection.
222 A multimode fiber (Thorlabs, Inc., 200 μm in diameter and 0.39 in numerical
223 aperture) coupled to an objective lens (Olympus Inc,10×, NA 0.3) is used for optical
224 transmission. The fluorescence signals are collected with a photomultiplier tube
225 (PMT) (Hamamatsu, Inc. R3896) after filtering by a GFP bandpass filter (Thorlabs,
226 Inc. MF525-39). An amplifier (C7319, Hamamatsu) is used to convert the current
227 output from the PMT to voltage signals, which are further filtered through a lowpass
228 filter (40 Hz cut-off; Brownlee 440, USA). The fluorescence signals are digitalized at
229 100 Hz and recorded by a Power 1401 digitizer and a Spike2 software (CED, UK).
230 Photometric data are exported and analyzed with MATLAB. The fluorescence signals
231 ($\Delta F/F_0$) are processed by averaging the baseline signal F_0 over a 4.5-s long control
232 time window, and presented as heatmaps or per-event plots. AUC (area under the
233 curve) of DA signal is used for statistical analysis. AUC is the integral of a curve that
234 describes the variation of DA signals during light stimulation.

235

236

237

References

1. Ding H, Lu L, Shi Z, Wang D, Li L, Li X*, et al.* Microscale optoelectronic infrared-to-visible upconversion devices and their use as injectable light sources. *Proc Natl Acad Sci U S A* 2018, **115**(26)**:** 6632-6637.
2. Li L, Liu C, Su Y, Bai J, Wu J, Han Y*, et al.* Heterogeneous Integration of Microscale GaN Light-Emitting Diodes and Their Electrical, Optical, and Thermal Characteristics on Flexible Substrates. *Adv Mater Technol* 2018, **3**(1)**:** 1700239.
3. Liu C, Zhang Q, Wang D, Zhao G, Cai X, Li L*, et al.* High Performance, Biocompatible Dielectric Thin-Film Optical Filters Integrated with Flexible Substrates and Microscale Optoelectronic Devices. *Adv Opt Mater* 2018, **6**(15)**:** 1800146.
4. Gebhart SC, Lin WC, Mahadevan-Jansen A. In vitro determination of normal and neoplastic human brain tissue optical properties using inverse adding-doubling. *Phys Med Biol* 2006, **51**(8)**:** 2011-2027.
5. Zhao Y, Liu C, Liu Z, Luo W, Li L, Cai X*, et al.* Wirelessly Operated, Implantable Optoelectronic Probes for Optogenetics in Freely Moving Animals. *IEEE Trans Electron Devices* 2019, **66**(1)**:** 785-792.
6. Peirson SN, Brown LA, Pothecary CA, Benson LA, Fisk AS. Light and the laboratory mouse. *J Neurosci Methods* 2018, **300:** 26-36.
7. Klapoetke NC, Murata Y, Kim SS, Pulver SR, Birdsey-Benson A, Cho YK*, et al.* Independent optical excitation of distinct neural populations. *Nat Methods* 2014, **11**(3)**:** 338-346.
8. Govorunova EG, Sineshchekov OA, Janz R, Liu X, Spudich JL. Natural light-gated anion channels: A family of microbial rhodopsins for advanced optogenetics. *Science* 2015, **349**(6248)**:** 647.
9. Mahn M, Gibor L, Patil P, Cohen-Kashi Malina K, Oring S, Printz Y*, et al.* High-efficiency optogenetic silencing with soma-targeted anion-conducting channelrhodopsins. *Nat Commun* 2018, **9**(1)**:** 4125.
10. Sun F, Zhou J, Dai B, Qian T, Zeng J, Li X*, et al.* Next-generation GRAB sensors for monitoring dopaminergic activity in vivo. *Nat Methods* 2020, **17**(11)**:** 1156-1166.
11. Wu X, Dong X, Wu Z, Cao H, Niu D, Qu J*, et al.* A novel method for purification of recombinant adenoassociated virus vectors on a large scale. *Chinese Sci Bull* 2001, **46**(6)**:** 485-488.
12. Lu L, Ren Y, Yu T, Liu Z, Wang S, Tan L*, et al.* Control of locomotor speed, arousal, and hippocampal theta rhythms by the nucleus incertus. *Nat Commun* 2020, **11**(1)**:** 1-16.
13. Lu L, Wang R, Luo M. An optical brain-to-brain interface supports rapid information transmission for precise locomotion control. *Sci China Life Sci* 2020, **63**(6)**:** 875-885.